UNIVERSIDADE DE LISBOA
FACULDADE DE CIÊNCIAS
DEPARTAMENTO DE ENGENHARIA GEOGRÁFICA, GEOFÍSICA E ENERGIA

Seismicity of the gulf of Cadiz:
Insights from the joint analysis of OBS and land seismic data

Daniela Sofia Da Paz Bolrão

Mestrado em Ciências Geofísicas
Especialização em Geofísica Interna

Dissertação orientada por:
Professora Doutora Susana Inês da Silva Custódio

2016

For those who look into science as a way of getting nothing but true happiness.

Agradecimentos/Acknowledgments

Muitos são os nomes que conduziram o meu até à capa desta dissertação. Tudo o que aqui escrevo é resultado da minha passagem pelas vossas vidas, de onde pude retirar ideias e criar as minhas próprias. Só por isso, obrigada. Todos estes nomes são importantes, mas apenas alguns ficarão aqui registados.

To **Dr. Ingo Grevemeyer**, thank you for sharing the data from the OBS stations, e ao **Doutor Carlos Corela**, obrigada por me ensinar sobre estas. To **Dr. Pierre Arroucau**, thank you, your work improved mine. Ao **Professor Luis Matias**, obrigada por me mostrar o fantástico mundo debaixo dos meus pés, e ao **Professor Ricardo Trigo**, obrigada por me permitir chegar mais longe e explorar, viver esse mundo. À **Professora Graça Silveira**, que está sempre por perto quando decido alargar o meu estreito espectro de conhecimento, obrigada por estar do meu lado. Ao **Manuel Afonso Loureiro**, que me foi brindando todos os dias com palavras sábias, obrigada, vais chegar longe. E ao colegas **Miguel**, **Martin**, **Mariana**, **Carlos** e **Susana**, obrigada, aprender ao vosso lado teve o seu encanto e fez-me sorrir em muitos momentos.

Espero que na vida de cada um haja sempre uma **Rita**, **Laura**, **Sofia** e **Filipa**, e ainda um **David** e **Renan**. Uma vida sem eles seria chata, sem sabor, sem ritmo. Obrigada por afectarem a minha com a vossa.

E para terminar, obrigada a quatro gigantes:

Susana Custódio, minha orientadora. Obrigada pelas ideias e palavras, pelo apoio e força que me foste passando ao longo deste tempo que partilhámos juntas. Aprendi muito, cresci muito. Achava que a ciência era um conto de fadas, que era um mundo perfeito. Mostraste-me que não o era, que há dias bons e dias maus, e que temos de ter capacidade para saber agradecer pelos dois. No fim de contas, continua a ser mágico. Obrigada não só por isto, mas também por me ajudares a chegar mais longe. As tuas palavras vão permitir que eu descubra um mundo novo, onde me vou assustar muitas vezes. No entanto, tenho a certeza de que enquanto me lembrar da tua postura, vai correr tudo bem, vai estar tudo bem. És um exemplo, obrigada.

Catarina Matos, minha orientadora não oficial. Obrigada por todos os momentos que passámos a falar do mundo comum que nos rodeia. Trabalhar ao teu lado, partilhar contigo os meus medos e vitórias, foi das coisas que mais sã me deixou ao longo deste tempo. Darás uma excelente orientadora um dia.

Famíla, o meu pilar. Nunca um “obrigada” pareceu tão pouco para expressar aquilo que sinto. Felizmente um olhar basta-vos, vocês sabem sempre o que penso. E ao **Casaca**, claro, que sorri todos os dias, e eu sorrio com ele.

E mais não digo, as palavras seriam sempre poucas. Os actos serão sempre melhores.

Resumo

O golfo de Cádiz está localizado no sudoeste da Península Ibérica, na fronteira entre as placas tectónicas Euroasiática e Africana, onde a convergência é acomodada de forma difusa por uma rede de falhas activas. Esta região sismogénica é conhecida pela sua capacidade de gerar sismos de elevada magnitude, como o de 28 de Fevereiro de 1969 ($M_S \approx 7.9$) ou o grande terremoto de Lisboa de 1 de Novembro de 1755 ($M_W \approx 8.7$). O objectivo deste trabalho é compreender melhor a distribuição da sismicidade e falhas que estão actualmente activas na zona.

Para estudar a sismicidade utilizámos seis meses de dados, obtidos a partir de uma rede temporária de vinte e quatro Ocean Bottom Seismometers (OBS), colocados a sudoeste da Península Ibérica, entre 20 de Janeiro e 21 de Julho de 2010, no âmbito do projecto internacional TOPO-MED. Adicionalmente, de forma a complementar estes dados, a melhorar geometria da rede e consequentemente minimizar os erros de localização hipocentral, usámos dados de quarenta e nove estações em terra. Estas estações fazem parte de redes permanentes e temporárias, localizadas a sul de Portugal, sudoeste de Espanha e noroeste de Marrocos. A região a ser aqui objecto de estudo foi limitada a uma área rectangular de $4.5° \times 2.0°$, de $11.0°$O a $6.5°$O e de $35.0°$N a $37.0°$N, e ao tempo de operação dos OBS. Fizemos uma análise da completude e identificação das componentes sísmicas destas estações, de onde concluimos que, à excepção de uma estação que dispunha apenas do hidrofone, OBS 35, todas as outras tinham dados disponíveis para a análise. Para reduzir o tempo de computação dos processos de detecção e localização, tanto os dados de OBS como os de terra foram nesta primeira fase de análise, decimados para 50 Hz.

Como estamos a analisar seis meses de dados contínuos de setenta e três estações, detectar as fases sísmicas de forma manual seria um processo muito dispendioso em termos de tempo. Decidimos por isso adoptar uma abordagem automatizada. Utilizámos o algoritmo Lassie (Heimann et al., 2015), que permite a detecção de chegadas coincidentes com energia sísmica às estações, e baseia-se nas funções características das formas de onda. Este método foi utilizado porque os resultados que fornece podem ser directamente usados num programa de localização, como o LOKI (Grigoli et al., 2013), sem passar pela tarefa de picar e identificar as chegadas sísmicas. O catálogo fornecido pelo Lassie com informações sobre o tempo a que os eventos foram detectados, as suas coordenadas e o valor de amplitude que as detecções obtiveram, tem de ser analisado manualmente para rejeitar potenciais falsos alarmes que tenham sido registados. Estes falsos alarmes podem ser acontecimentos locais, problemas no sensor, mudança de dia ou falta de dados. Todos estes têm uma assinatura particular e de elevada amplitude, que ao distinguir-se tanto do resto do ruído, são considerados como sismos. O algoritmo Lassie tem como parâmetros de entrada a grelha espacial, a largura de banda do filtro a aplicar aos dados, a velocidade aparente das ondas que se movem nesta grelha, e o valor limite acima do qual se pode considerar ter-se detectado um sismo. Este último parâmetro é o mais difícil de determinar e não é imediato. Para saber qual o que melhor serve os dados usados é necessário fazer um teste prévio. Fizemos esta pré-análise a uma amostra de teste de 10% dos dados, o que corresponde a uma análise de dezanove dias, escolhidos aleatoriamente entre o período de 2010-05-07 e 2010-05-25. Após analisar manualmente todas as detecções do catálogo que caem dentro da região de estudo com o Snuffler (Heimann, 2012), assumimos que o valor de 110.0 de amplitude é um bom compromisso entre detectar um número considerável de sismos, e evitar a detecção de demasiados falsos alarmes. Este valor foi aplicado aos seis meses de dados e todas as detecções do catálogo que caíram dentro da zona de estudo foram novamente inspeccionadas manualmente com o Snuffler. Foram detectados 153 sismos dentro da área de interesse.

Para o processo de localização destes sismos, utilizámos dois programas, o LOKI e o NonLinLoc (Lomax et al., 2000). Antes de utilizar o LOKI, fizemos uma pré-análise às formas de onda, para retirar

dos eventos as formas de onda que apresentassem uma razão sinal-ruído muito baixa. Neste processo também ajustámos as janelas temporais à duração do sismo, para evitar que o LOKI localizasse ruído coerente. Com esta análise foi possível perceber que tanto as estações de OBS, como as da rede sísmica XB, não iriam contribuir de forma significativa para a localização dos sismos, visto apresentarem uma razão sinal-ruído baixa.

O LOKI tem a vantagem de não necessitar de um catálogo de fases, o que permite trabalhar bem com formas de onda cujas chegadas P e/ou S sejam emergentes. O programa utilizou uma grelha espacial de 520 km × 370 km × 80 km a partir do ponto 11.0°O, 35.0°N e fez uso da razão entre a *short-time-average* e a *long-time-average* (STA/LTA), por forma a construir uma matriz de coerência a partir da qual as localizações podem ser inferidas. Este programa foi utilizado com dois modelos de velocidades diferentes, um 1D (Geissler et al., 2010) e outro 3D (Arroucau and Custódio, 2015). Mostra-se que a utilização do modelo de velocidades 3D permite obter hipocentros mais robustos. Por inspecção visual, o modelo 3D apresenta maiores valores de coerência no ponto que é considerado uma localização, e os pontos na vizinhança deste têm valores de coerência muito menores. Para mais, para cada evento calculámos a área que era ocupada por 95% do valor da coerência máxima. Somámos todas as áreas e o modelo 1D apresenta uma área de 66809 km^2, enquanto que o modelo 3D tem apenas 43851 km^2, valor bastante inferior. O LOKI tem a desvantagem de ser susceptível a localizar ruído coerente, e como também não apresenta os erros de localização, como RMS, GAP ou comprimento do semi-eixo maior da elipse, decidimos utilizar outro método, como o NonLinLoc.

O NonLinLoc é um conjunto de programas (Vel2Grid, Grid2Time e NLLoc) que utiliza técnicas não lineares para fazer a localização dos hipocentros. O NLLoc necessita de um catálogo de fases picadas e identificadas, que foi construído previamente com o Snuffler. Para a localização utilizámos o modelo de velocidades 3D e o algoritmo de Oct-Tree Importance Sampling. Este algoritmo baseia-se no cálculo da função de densidade de probabilidade, em células que vão sendo sucessivamente divididas em oito partes iguais. Conseguimos localizar 61 sismos dentro da área de estudo, com RMS $\leq$ 1.0 segundos, comprimento do semi-eixo maior da elipse $\leq$ 10 km, e GAP $\leq$ 220°. A sismicidade está localizada até cerca de 60 km de profundidade. Os resultados obtidos foram comparados com as localizações reportadas por Grevemeyer et al. (2016) e pelo IPMA, obtidas para o mesmo período de tempo. Em ambos os casos, mostrámos que com a utilização de dados de OBS e um modelo de velocidades 3D, consegue-se localizar um maior número de sismos de forma mais robusta.

Analisámos também os eventos do catálogo sísmico para estimar magnitudes. Começámos por remover a resposta instrumental das formas de onda, o que implica saber os pólos, zeros, sensibilidade e ganho dos sensores. Como esta informação não estava disponível para os instrumentos dos OBS e algumas estações em terra, só foi possível remover a resposta de 33 das 73 estações. Recorremos à fórmula de Carrilho and Vales (2009) e concluimos que o intervalo de magnitudes varia entre 0.0 e 4.3. Os sismos de maior magnitude ($\geq$ 3.0) podem ser encontrados até cerca de 40 km de profundidade, enquanto que sismos de magnitude menor, entre 2.0 e 3.0, podem ser encontrados até cerca de 60 km.

Estudámos ainda a similaridade entre formas de onda para determinar se existem aglomerados de eventos. Estes terão de apresentar os mesmos mecanismos focais, os mesmos efeitos de sítio e o mesmo padrão de radiação, indicativo de terem sido gerados na mesma estrutura tectónica. Para poderem apresentar o mesmo efeito de sítio, as ondas sísmicas têm de percorrer caminhos semelhantes, como tal, a correlação é feita apenas para os eventos registados na mesma estação. Utilizámos bibliotecas do Python/Obspy (Beyreuther et al., 2010) para analisar as componentes Z de cada evento, em torno da chegada da onda P, 0.6 segundos antes desta e 1.0 segundo depois. Embora com poucos eventos, apenas 61, conseguimos encontrar dois aglomerados, ambos com 4 eventos com coeficientes de correlação

maiores ou iguais a 0.8. Um destes aglomerados encontra-se perto de falhas já mapeadas, enquanto que o outro encontra-se numa zona sem qualquer falha mapeada. Para se conseguir inferir alguma conclusão, é necessário repetir a mesma análise mas para um período de tempo mais alargado.

Palavras-chave: Golfo de Cádiz, Sismos, Detecções, Localizações 3D, Aglomerados.

Abstract

The gulf of Cadiz is a seismogenic region located southwest of the Iberia Peninsula, in the Eurasian-African plate boundary, where plate convergence is accommodated in a diffuse way along a complex network of faults. This region is known for its ability to cause earthquakes of large magnitude, such as the great Lisbon earthquake of November 1, 1755.

With the aim of better understanding faults that are currently active in the region, we studied the seismicity in a particular area of $4.5° \times 2.0°$, from $11.0°$W to $6.5°$W and from $35.0°$N to $37.0°$N, in the gulf of Cadiz, from January, 20 to July, 21 of 2010. We focused on using data from 24 OBS, deployed within this region and at this time under the TOPO-MED project (Grevemeyer, 2011). In order to improve the geometry of the network we further used 49 land stations, from temporary and permanent networks, located in south of Portugal, southwest of Spain and northwest of Morocco.

We used a new methodology to study the seismicity of this region. The detection of earthquakes of low magnitude was performed using the algorithm Lassie (Heimann et al., 2015). We further used a 3D velocity model (Arroucau and Custódio, 2015) to locate the 61 earthquakes detected within the study area. Our locations are compared with others obtained by studies made for the same period, by Grevemeyer et al. (2016) and by Portuguese Sea and Atmosphere Institute (IPMA), both using 1D velocity models. We show that hypocentres resulted from the 3D velocity model analysis are better constrained.

We also estimated local magnitudes, which range between 0.0 and 4.3, and searched for clusters of events that belong to the same tectonic structure. We were able to find two clusters, with 4 events each and cross-correlation coefficients higher than or equal to 0.8. While one of these is located near faults, the other cluster is located in an area far way from the mapped faults.

Keywords: Gulf of Cadiz, Earthquakes, Detections, 3D Locations, Clusters.

Contents

Agradecimentos/Acknowledgments iii

Resumo v

Abstract ix

List of Tables xiii

List of Figures xv

1 Introduction 1

1.1 Brief tectonic setting 1

2 Data 3

2.1 Case study 3

2.2 Seismic data 3

2.3 OBS seismic components 4

3 Detections of earthquakes 7

3.1 Lassie method and definition of parameters 7

3.2 Determination of the threshold 8

4 Locations of earthquakes 13

4.1 Preparing the waveforms for LOKI 13

4.2 LOKI 14

4.2.1 LOKI results: comparison between 1D and 3D velocity models 15

4.3 NonLinLoc 18

4.3.1 NonLinLoc results with 3D velocity model 19

4.3.2 Comparison between NonLinLoc with 3D velocity model and Grevemeyer et al. (2016) study 20

4.3.3 Comparison between NonLinLoc with 3D velocity model and IPMA results . . . 21

5 Analysing the seismic catalogue: magnitudes and waveform similarity 23

5.1 Determination of magnitudes 23

5.2 Cross-correlation of waveforms 24

6 Conclusion 29

References 31

A Stations metadata information 33

B Networks of the seismic stations 37

C Velocity models 39

C.1 3D velocity model 39

C.2 1D velocity model 40

List of Tables

1 Information about OBS stations 34
2 Information about land stations 35
3 1D velocity model from Geissler et al. (2010), with a Vp/Vs ratio of 1.77. 40

List of Figures

1.1 Adapted from Duarte et al. (2014). B: Location of gulf of Cadiz. ATJ—Azores triple junction; AGFZ— Azores-Gibraltar fracture zone. C: Tectonic map of southwest Iberia margin. Gray arrows show Gibraltar Arc movement; white arrows show Africa-Eurasia WNW-ESE convergence. 2

2.1 Map of gulf of Cadiz and boundaries of the region to be studied between January, 20 and July, 21 of 2010. The seismic stations (triangles) are colour coded by network. 3

2.2 Completeness of each component while stations were operating: each triangle represents, from left to right, component 1, 2, 3 and 4 of the stations, with sampling frequency of 50 Hz (triangles) or 100 Hz (inverted triangles). The colours green (100 %), yellow (97.3 %), orange (65.4 %) and red (0 %) represent the completeness of data of each component. 4

2.3 Comparison between SEISAN file with seismic components discriminated (left) and *mseed* data file (right), for station 48 (short-period seismometer – 50 Hz): hydrophone is channel 1, vertical is channel 4, and horizontal components are channels 2 and 3. Unfiltered data of 2010-02-02, from 05:56:15 to 05:58:04.99. 5

2.4 Comparison between SEISAN file with seismic components discriminated (left) and *mseed* data file (right), for OBS 34 (broad-band seismometer – 100 Hz): hydrophone is channel 1, vertical is channel 2, and horizontal components are channels 3 and 4. Unfiltered data of 2010-02-02, from 05:56:15 to 05:58:04.99. 5

3.1 Rectangular grid used in Lassie, of 600 km × 600 km centred in (CG) 7.5°W, 36.5°N, which includes all the seismic stations (grey triangles). 8

3.2 Map with seismic stations (grey triangles) and locations of the events (red dots) obtained with a detection threshold of 80.0, for 10% of data (between 2010-05-07 and 2010-05-25). Lassie detected 585 events but only 297 of these fell into the study area. 9

3.3 Example of an earthquake: detection with value of 322.53, at 03:11:39.000 of 2010-03-31. Data filtered between 5 and 15 Hz. 9

3.4 Example of a false positive: detection with value of 156.247 in a change of day, from July 4 to July 5, at 23:58:45.000. The merge of data from these two days around 00:00, generates a signal with high amplitude. 10

3.5 Example of a false positive: detection value of 172.84, at 04:33:17 of 2010-02-12, due to lack of data (white spaces). When we have data again, the first signal has a very strong signature with high amplitude. 10

3.6 Number of detections versus threshold, for (a) false positives and (b) earthquakes. A threshold of 110.0 is a good compromise between detecting earthquakes and avoiding a large number of false positives. 10

4.1 Data from each station used to locate earthquakes, using LOKI. This determination was based on visual analysis to the waveforms of each event: 0 (black) cannot locate, 153 (white) can locate all the earthquakes. 13

4.2 2D projection of the used grid of 520 km × 370 km × 80 km, from point 11.0°W, 35.0°N, and three-component seismic stations (grey triangles) from which data can be used in LOKI. 14

4.3 Values of maximum coherence for events located with LOKI, with 1D velocity model (left) and 3D velocity model (right). With the last one, higher values of coherence can be reached. 15

4.4 Values of maximum hypocentre error for events located with LOKI, with 1D velocity model (left) and 3D velocity model (right). With the last one, we have more earthquakes with lower erros. 15
4.5 Map with the locations of the earthquakes with 1D velocity model (green dots) and 3D velocity model (red dots), with LOKI. Earthquakes with the same origin time are linked. 16
4.6 Distribution of distance between same events (left) and difference of depth for same events (right), located with LOKI with 1D and 3D velocity models. 16
4.7 Location of the earthquake occurred on 2010-02-28 at 16:32:49, using LOKI with 1D (above) and 3D (below) velocity models. From left to right we see cross sections of the coherence matrix in X-Y, X-Z and Y-Z plans. It is clear that 3D velocity model provides more accurate locations. 17
4.8 Location of the earthquake occurred on 2010-03-21 at 05:27:10, using LOKI 1D (above) and 3D (below) velocity models. From left to right we see cross sections of the coherence matrix in X-Y, X-Z and Y-Z plans. It is clear that 3D velocity model provides more accurate locations. 17
4.9 2D projection of the used grid of $580 \times 570 \times 80$ km from point 11.0°W, 34.0°N, and seismic stations (grey triangles) used in NonLinLoc. 18
4.10 Distribution of RMS values (left) and GAP (right), of the 153 earthquakes located with NonLinLoc - 3D model. For convenience of visualization, from RMS histogram we removed ten outliers, varing between 12.3328 and 436.366 seconds. 19
4.11 Distribution of errors of the 153 earthquakes located with NonLinLoc - 3D model: length of semi-major axis of the epicentre location (left) and error in depth (right). 19
4.12 Colour coded locations inside the study region, obtained with a 3D velocity model in NonLinLoc: all the earthquakes (dots) have RMS $\leq$ 1.0 s and a length of semi-major axis $\leq$ 10 km. Grey dots represent earthquakes with $180° < \text{GAP} \leq 220°$, and the blue dots represent the ones with GAP $\leq$ 180°. The seismic stations are also colour coded by the number of times that each one was used to locate an earthquake. 20
4.13 Locations of the 26 common earthquakes in the catalogues obtained by Grevemeyer et al. (2016) (green dots) and by NonLinLoc - 3D model (red dots). Earthquakes with the same origin time are linked. 21
4.14 Comparison between 26 common earthquakes in the catalogues obtained by NonLinLoc - 3D model and Grevemeyer et al. (2016): distribution of distance between same epicentres (left) and differences of depth of same events (right). 21
4.15 Locations of the 58 common earthquakes in the catalogues obtained by NonLinLoc - 3D model (red dots) and IPMA (green dots). Earthquakes with the same origin time are linked. 22
4.16 Result of the comparison between hypocentre locations obtained with NonLinLoc - 3D model and IPMA: distribution of distance between same epicentres of events (left) and differences of depth of same events (right). 22
5.1 Distribution of local magnitudes of the 61 earthquakes located with NonLinLoc - 3D model, colour coded to help rapidly visualise the map in Figure 5.2. 23
5.2 Map with stations used for estimation of magnitudes, and earthquakes colour coded according to magnitude. 24
5.3 Histogram resulted from the cross-correlation analysis. CC stands for cross-correlation coefficient. 25

5.4 Example of a cross-correlation coefficient of 0.86 in station ESPR, for the pair of events occurred on 2010-03-24T21:23:20 (9.871°W, 36.413°N) and 2010-07-04T18:15:04 (7.193°W, 36.683°N). 25
5.5 Example of a cross-correlation coefficient of 0.90 in OBS 40, for the pair of events occurred on 2010-02-06T22:00:07 (8.591°W, 36.040°N) and 2010-06-01T10:46:30 (7.844°W, 36.481°N). 25
5.6 Map with a cluster of events (purple dots) detected by station ESPR (red triangle) with NonLinLoc - 3D model. Grey dots are the other locations made by this station. 26
5.7 Map with a cluster of events (purple dots) detected by station PBDV (red triangle), with NonLinLoc - 3D model. Grey dots are the other locations made by this station. 26
5.8 Map of geologically mapped faults and the two clusters detected by stations ESPR (green dots) and PBDV (orange dots). Yellow dots represent the other earthquakes located with NonLinLoc - 3D model, that do not belong to any cluster. 27
C.1 Region included by the velocity model of Arroucau and Custódio (2015), and boundaries of the regions of interest used in LOKI (green rectangle) and NonLinLoc (blue rectangle). 39

1 Introduction

The offshore Cadiz basin is located along the Eurasian-African plate boundary, west of the Gibraltar strait, in a region of diffuse deformation where plate convergence is accommodated by a complex network of faults (e.g. Terrinha et al., 2009; Duarte et al., 2014). This region is known for its ability to unleash earthquakes of large magnitude, such as the February 28, 1969 ($M_S \approx 7.9$) or the great Lisbon earthquake of November 1, 1755 ($M_W \approx 8.7$), which affected all the south and southwest coast of Portugal, causing a high number of casualties (Simões et al., 1992). It is therefore important to monitor this seismogenic area in order to understand the tectonics, active faults and earthquake activity, which can be useful, for instance, to update seismic hazard maps for the region.

This area is constantly monitored by the Portuguese Sea and Atmosphere Institute, I. P. (IPMA) and the accuracy of the locations reported is influenced by the geometry of the network used (e.g. Husen and Hardebeck, 2010). As IPMA relies on land stations only, the hypocentres of events located offshore will have large azimuthal gaps, and the accuracy of the location is reduced. In order to minimize this problem, Ocean Bottom Seismometers (OBS) stations can be used to complement land stations. For instance, in the first six months of 2010, 24 OBS stations were deployed in the gulf of Cadiz region, under the TOPO-MED project (Grevemeyer, 2011). This project was carried in order to investigate the relations between surface/shallow processes and deep lithospheric/mantle structures and dynamics. Also, it was taken in order to understand about the tectonic and morphological evolutions in the coastal regions surrounding the western Mediterranean.

In this study we employ a new automated methodology to detect and locate earthquakes in the gulf of Cadiz, in a particular area from 11.0°W to 6.5°W and from 35.0°N to 37.0°N. We used six months of data, from January, 20 to July, 21 of 2010, from the OBS deployed in this region and at this time under the TOPO-MED project, and land stations from temporary and permanent networks, located in south of Portugal, southwest of Spain and northwest of Morocco (in Section 2).

The results of this study are compared with the locations reported by IPMA and with locations already reported for this region by Grevemeyer et al. (2016). The detection of earthquakes by Grevemeyer et al. (2016) was based on a short-term-average to long-term-average ratio (STA/LTA) triggering approach, and their locations were performed using picking and identification of phases, from the same OBS data, and less land stations than used in our study. They used several 1D velocity models (one of them from Geissler et al., 2010), which may not be suited to give robust locations in this complex area.

In this work, earthquakes were detected using Lassie (Heimann et al., 2015), an approach recently developed that is based on characteristic functions of waveforms (in Section 3). For the first time in this area, the earthquakes are located with a 3D velocity model from Arroucau and Custódio (2015), using LOKI (Grigoli et al., 2013) and NonLinLoc (Lomax et al., 2000). We also used the 1D velocity model from Geissler et al. (2010) with LOKI to evidence the differences between 1D and 3D velocity models (in Section 4). After this analysis, we determined the magnitudes of the located earthquakes using the equation proposed by Carrilho and Vales (2009), and analysed the waveform similarity between events in order to understand if they have similar source mechanisms (in Section 5).

1.1 Brief tectonic setting

The gulf of Cadiz is a complex region located in the Atlantic Ocean, in southwest of Iberia Peninsula (Figure 1.1B), located between the Eurasian and African tectonic plates, which are converging in WNW-ESE direction, at a rate of 4 mm/year (DeMets et al., 2010).

This seismogenic region is very active and low-magnitude earthquakes are frequently reported by IPMA. However, this region is also known for the ability to unleash earthquakes of large magnitude (e.g. February 28, 1969 and November 1, 1755).

The region we are interested in studying range from 11.0°W to 6.5°W and from 35.0°N to 37.0°N. This area is characterized by WNW-ESE–striking dextral strike-slip faults, known as the SWIM fault system. In our study we used data from seven OBS stations (37 – 43) located on top of one SWIM fault, and five OBS (32 – 35, 44) on top another.

Also, the study region includes active tectonic systems such as the Marquês de Pombal, S. Vicente, Cadiz and Portimão faults, and the Portimão Pop-Up. The last one is monitored by OBS 45 – 54.

Most of the OBS stations are located on top of the accretionary wedge. This has a maximum thickness of 15 km (Thiebot and Gutscher, 2006) and is formed by sediments between 0.2 km to 2 km of Late Miocene to Plio-Quaternary age (Zitellini and et al., 2009).

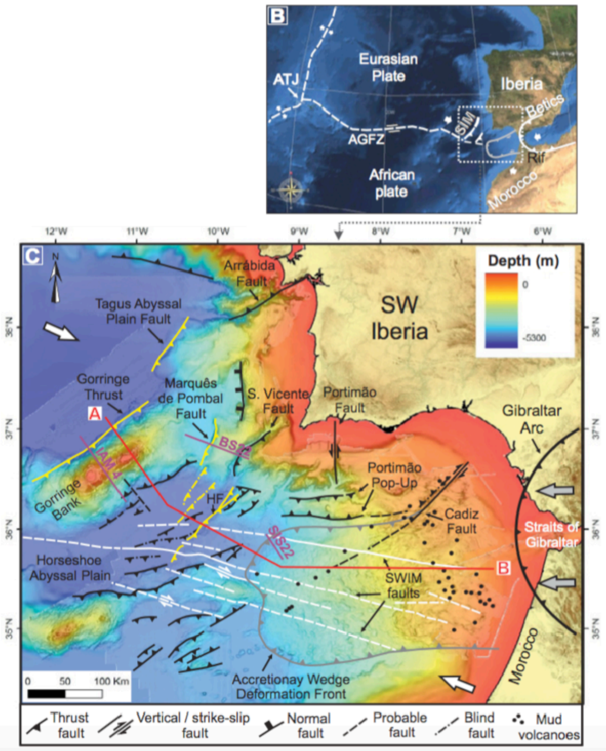

Figure 1.1: Adapted from Duarte et al. (2014). B: Location of gulf of Cadiz. ATJ—Azores triple junction; AGFZ— Azores-Gibraltar fracture zone. C: Tectonic map of southwest Iberia margin. Gray arrows show Gibraltar Arc movement; white arrows show Africa-Eurasia WNW-ESE convergence.

The study made by Sallarès et al. (2011) in this region shows that there are three crustal domains. Near the Algarve cost line there is a continental crust with 28 – 30 km thick, followed by a $\sim$ 60 km wide zone where the crust thins from $\sim$ 25 km to $\sim$ 7 km. Finally after this, there is a 150 km wide segment of oceanic crust, of $\sim$ 7 km thick. In terms of seismic activity, a recent study (Grevemeyer et al., 2016) reports occurrences in the lower crust and upper mantle, until depths around 40 km. A different study, made by Stich et al. (2005), reports deeper earthquakes, until 60 km.

2 Data

2.1 Case study

In order to study the seismic activity in the gulf of Cadiz, we used data from 24 OBS deployed under the TOPO-MED project (Grevemeyer, 2011), complemented by data from 49 land stations, from temporary (8A, XB) and permanent (ES, IP, LX, PM, WM) networks, located in south of Portugal, southwest of Spain and northwest of Morocco (Appendix A and B), as shown in Figure 2.1.

The study was limited to data from January, 20 to July, 21 of 2010, time at which the OBS stations were operating, and the region of interest was limited to a rectangular area of $4.5° \times 2.0°$, from $11.0°$W to $6.5°$W and $35.0°$N to $37.0°$N (Figure 2.1).

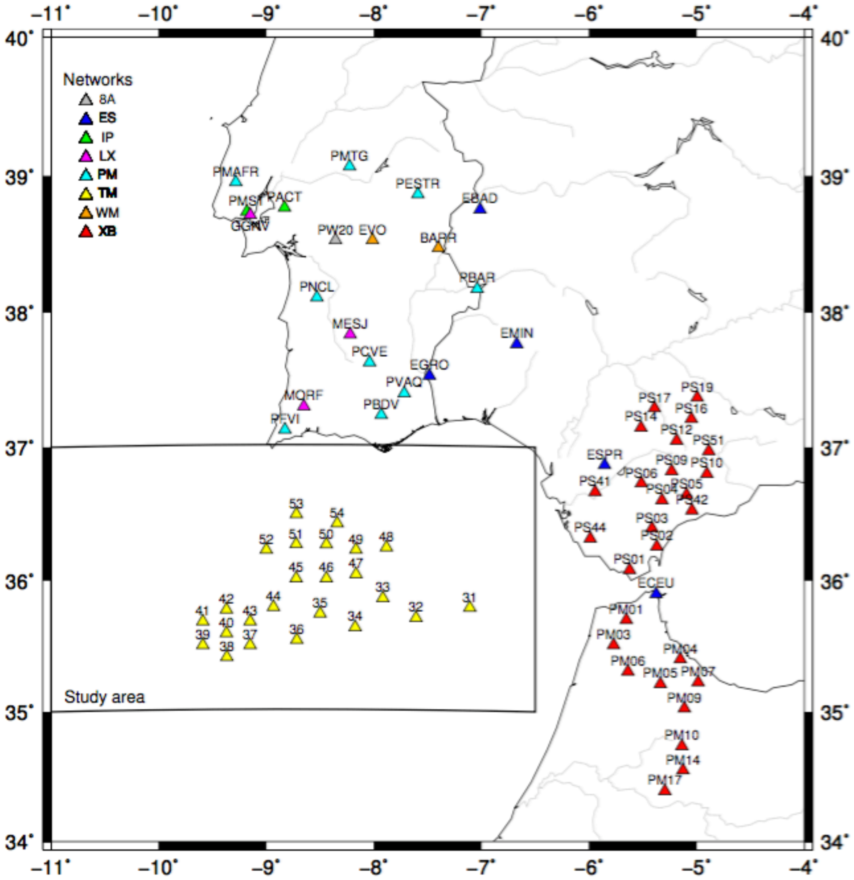

Figure 2.1: Map of gulf of Cadiz and boundaries of the region to be studied between January, 20 and July, 21 of 2010. The seismic stations (triangles) are colour coded by network.

2.2 Seismic data

The OBS data in *mseed* format, separated by station and continuum days, were kindly shared by Dr. Ingo Grevemeyer from GEOMAR – Helmholtz Centre for Ocean Research Kiel, Germany, who also shared some of the analysed waveforms in SEISAN format. The 24 instruments that recorded the data consisted in (Grevemeyer, 2011):

- 19 GEOMAR-OBS equipped with a 3-component short-period seismometer with a natural frequency of 4.5 Hz. These 19 OBS were operating at 50 Hz, and correspond to stations: 31, 33, 35, 37, 38, 39, 40, 41, 42, 43, 44, 45, 46, 47, 48, 49, 51, 53 and 54;

- 5 broad-band OBS operating a 3-component Guralp CMG-40T (60s) seismometer. These 5 OBS were operating at 100 Hz, and correspond to stations 32, 34, 36, 50 and 52.

To complement the OBS data, we used land stations from different networks, requested to the International Federation of Digital Seismograph Networks (FDSN) platform trough the package of Obspy (Beyreuther et al., 2010) **obspy.clients.fdsn.mass_downloader**. The stations of XB and IP networks acquired the data at 50 Hz, while all the others acquired at 100 Hz.

All the data were decimated to 50 Hz in order to reduce the number of points to be analysed. This way we minimized the overhead in the data processing time.

2.3 OBS seismic components

We identified the data effectively recorded during the OBS deployment, for the different components (1, 2, 3 and 4). This was done using **obspy-scan** tool of Obspy and the result of this analysis is shown in Figure 2.2.

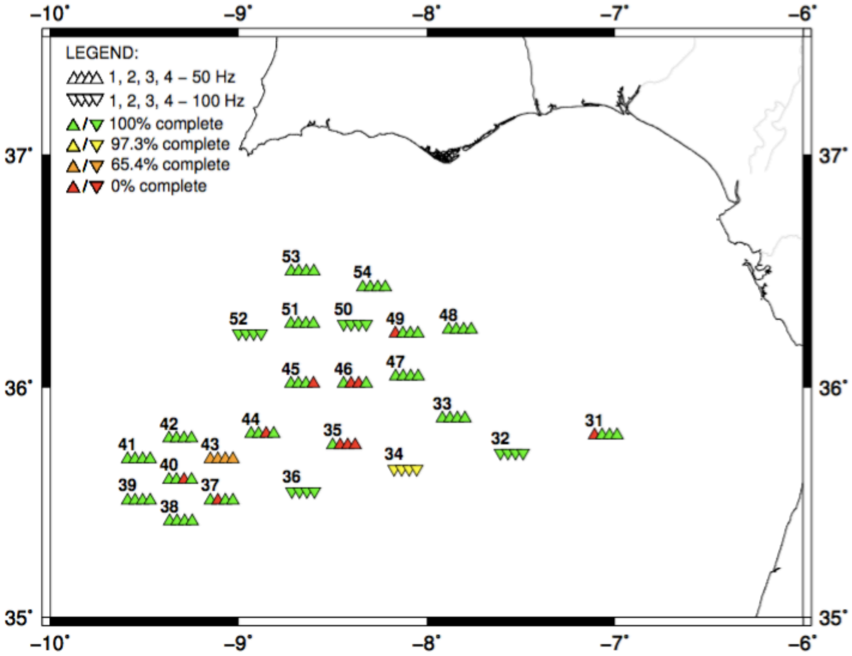

Figure 2.2: Completeness of each component while stations were operating: each triangle represents, from left to right, component 1, 2, 3 and 4 of the stations, with sampling frequency of 50 Hz (triangles) or 100 Hz (inverted triangles). The colours green (100 %), yellow (97.3 %), orange (65.4 %) and red (0 %) represent the completeness of data of each component.

To understand which component (1, 2, 3 and 4) corresponds to hydrophone, vertical and horizontal components, we plotted some of the raw data and compared it with the SEISAN data files that had the components discriminated. Two examples are shown in Figures 2.3 and 2.4. The analysis led us to conclude that for stations operating at:

- 50 Hz: hydrophone is channel 1, vertical is channel 4, and horizontal components are channels 2 and 3. Example for OBS 48 in Figure 2.3;

- 100 Hz: hydrophone is channel 1, vertical is channel 2, and horizontal components are channels 3 and 4. Example for station 34 in Figure 2.4.

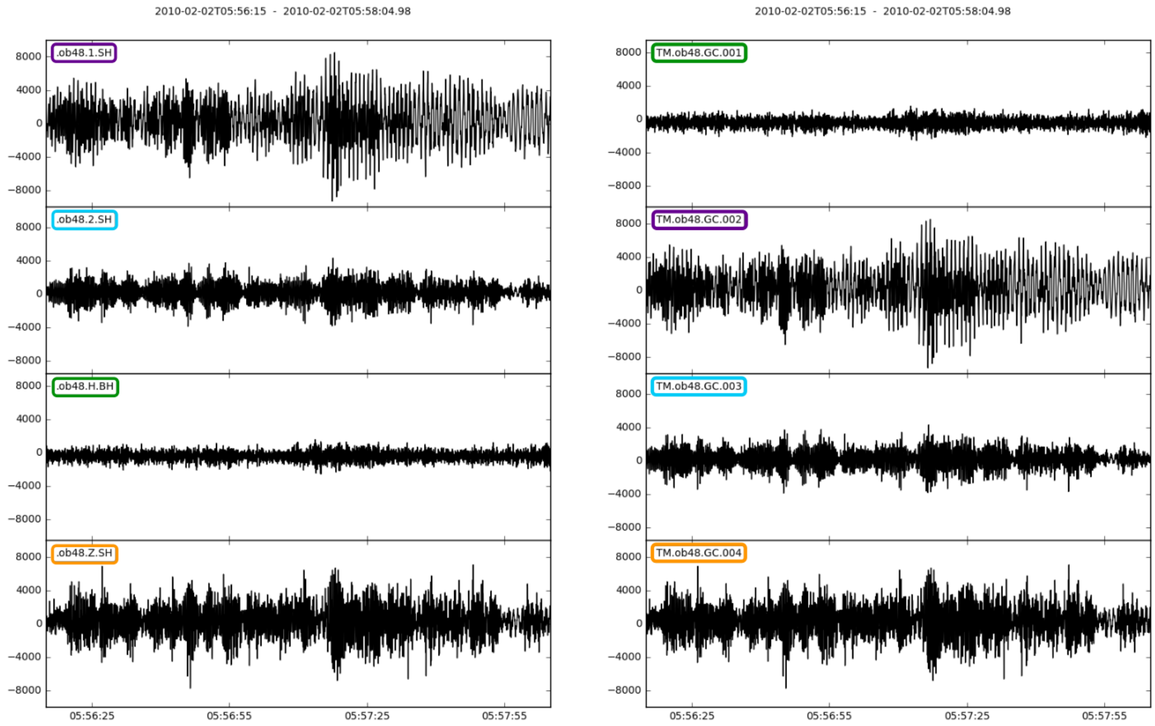

Figure 2.3: Comparison between SEISAN file with seismic components discriminated (left) and *mseed* data file (right), for station 48 (short-period seismometer – 50 Hz): hydrophone is channel 1, vertical is channel 4, and horizontal components are channels 2 and 3. Unfiltered data of 2010-02-02, from 05:56:15 to 05:58:04.99.

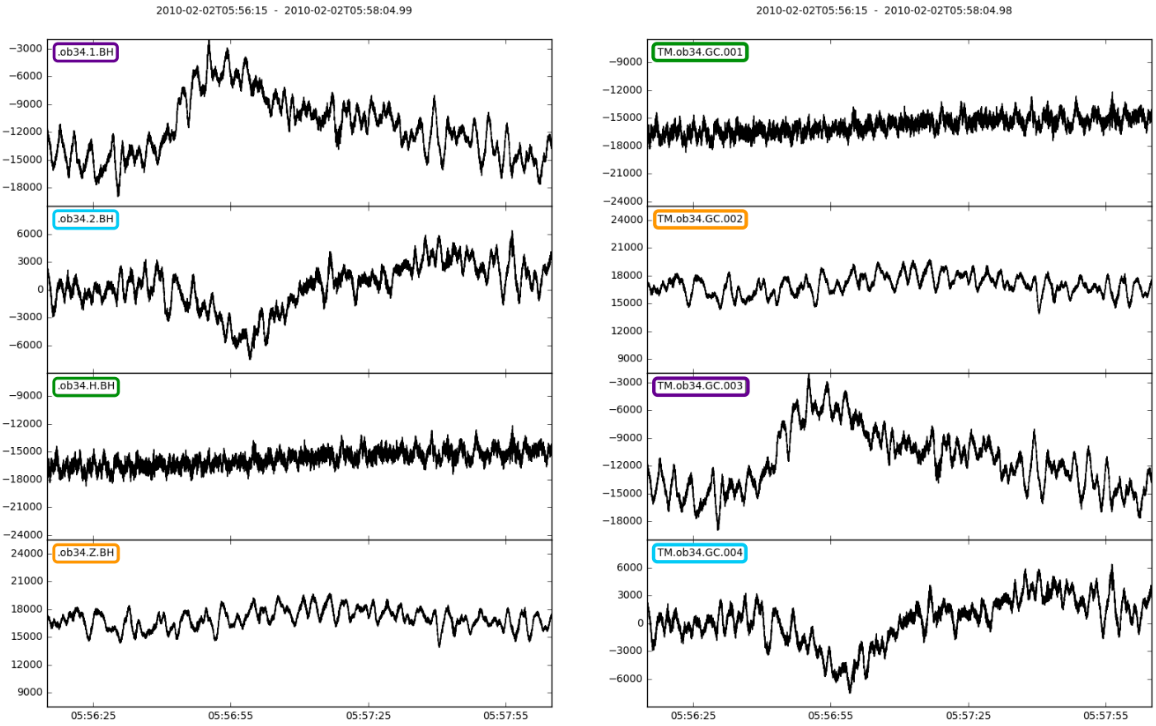

Figure 2.4: Comparison between SEISAN file with seismic components discriminated (left) and *mseed* data file (right), for OBS 34 (broad-band seismometer – 100 Hz): hydrophone is channel 1, vertical is channel 2, and horizontal components are channels 3 and 4. Unfiltered data of 2010-02-02, from 05:56:15 to 05:58:04.99.

After this analysis, we concluded that OBS 35 is the only station that cannot be used for the detection and location of the earthquakes, as its only available component is the hydrophone.

3 Detections of earthquakes

Detecting the earthquakes manually would be a time consuming work, specially as we have six months of continuous data from 73 stations. Therefore, it was decided to automate this process.

There are several recent automated methods that can detect earthquakes, for instance based on time-frequency analysis (e.g. Hafez et al., 2009) or by computing short-term average to long-term average ratio (STA/LTA) (e.g. Ross and Ben-Zion, 2014). In order to detect the events, we decided to use Lassie (Heimann et al., 2015), a method based on characteristic functions of the waveforms. The output of this program can be used directly by LOKI (Grigoli et al., 2013) to locate the earthquakes, without passing for the task of phase picking and identification.

3.1 Lassie method and definition of parameters

Lassie is a recent method, based on Python programming language, that allows the detection of coincident arrivals of seismic energy at recording stations. This method has several advantages, such as:

- no need to pick seismic phases;
- automatically builds a catalogue of seismic events with preliminary locations. This can be easily interfaced with LOKI, which provides more accurate locations;
- is computationally fast;
- is user-friendly since there are only few parameters that the user set.

These parameters that the user must choose according to the dataset used are: a spatial grid, the velocity of propagation, the filter bandwidth and the detection threshold. The last one is the most difficult parameter to define and it is advisable to run some tests to determine the most suitable one for the dataset (Subsection 3.2).

We started by defining the spatial grid that includes all seismic stations. This grid was centred in 7.5°W, 36.5°N, and extended 300 km to north, south, east and west, with 1.5 km between nodes (Figure 3.1). Lassie makes use of a spatial weighting matrix that gives higher weight to detections inside the grid and near its centre, and less weight to signals originated outside, such as teleseismic waves or even regional earthquakes.

The velocity at which the waves travel in the grid was chosen as 3.5 km/s. Once these parameters are defined, Lassie starts by scanning the continuous dataset in overlapping time windows and in each Lassie:

- First: computes a characteristic function for each station, based on the stacked amplitudes of the three components of the signal recorded, filtered between 0.1 Hz and 15 Hz.
- Second: considers each grid node as an epicentre. Then computes the expected arrival time of the waves at all stations and shifts each characteristic function accordingly. Then stacks them all, creating a single final function for each grid node.
- Third: detects a seismic event when the amplitude of this final function exceeds the threshold.
- Fourth: updates automatically the catalogue with the information of this new event, with its detection time, amplitude and epicentre coordinates.

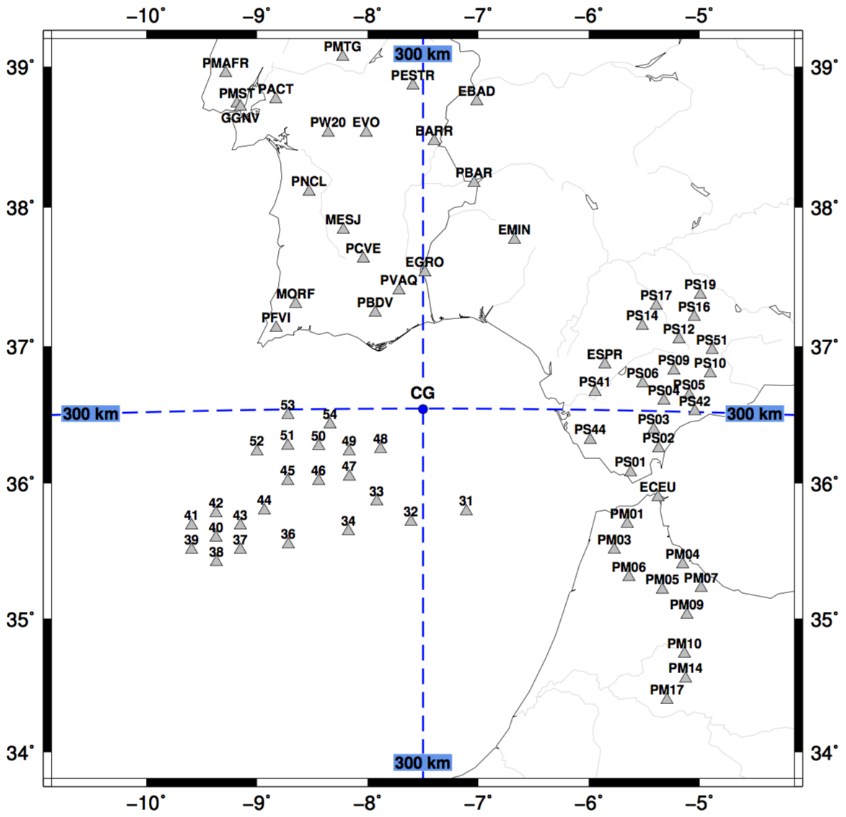

Figure 3.1: Rectangular grid used in Lassie, of 600 km × 600 km centred in (CG) 7.5°W, 36.5°N, which includes all the seismic stations (grey triangles).

In the end of this process, each detection in the catalogue has to be validated, in order to determine if it is in fact an earthquake or a false positive. This validation can be manually performed opening the catalogue with Snuffler (Heimann, 2012).

3.2 Determination of the threshold

The process to chose the suitable threshold for a given dataset is not straightforward, and can be divided in two parts.

First, an arbitrary value is used, and as a reference, we looked to the work done by Heimann et al. (2015), where the threshold value was 120.0. We chose a slightly smaller one of 80.0, as initial condition. To verify if this was a good value, we ran Lassie using only 10% of data, which corresponds approximately to 19 days, randomly selected between 2010-05-07 and 2010-05-25.

Second, a manual identification of the events in the created catalogue is made in order to detect false positives and earthquakes. We obtained 585 detections, but only 297 fell into the study region (rectangle on Figure 3.2). These were manually validated with Snuffler as earthquakes – if we saw a coherent arrival with two energy packets (P and S waves), at least in three stations (Figure 3.3) – or false positives. The change of days around 00:00 (Figure 3.4), lack of data (Figure 3.5) and local events are the main reasons to generate a false earthquake detection, as these signals produce peaks with energy capable to rise above the noise, and create characteristic functions of high amplitude.

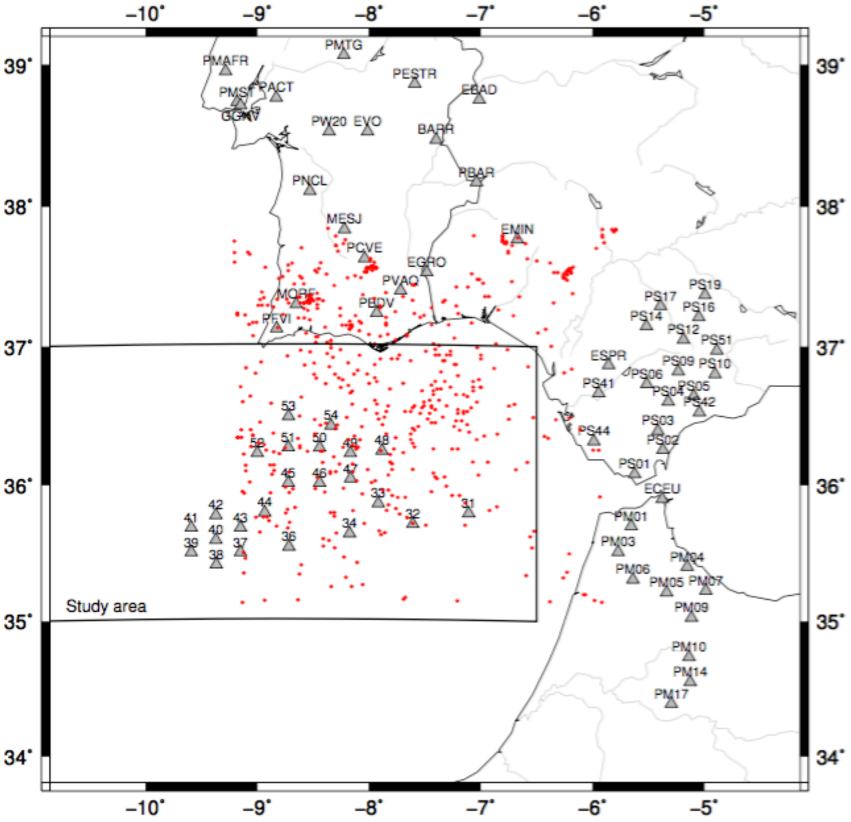

Figure 3.2: Map with seismic stations (grey triangles) and locations of the events (red dots) obtained with a detection threshold of 80.0, for 10% of data (between 2010-05-07 and 2010-05-25). Lassie detected 585 events but only 297 of these fell into the study area.

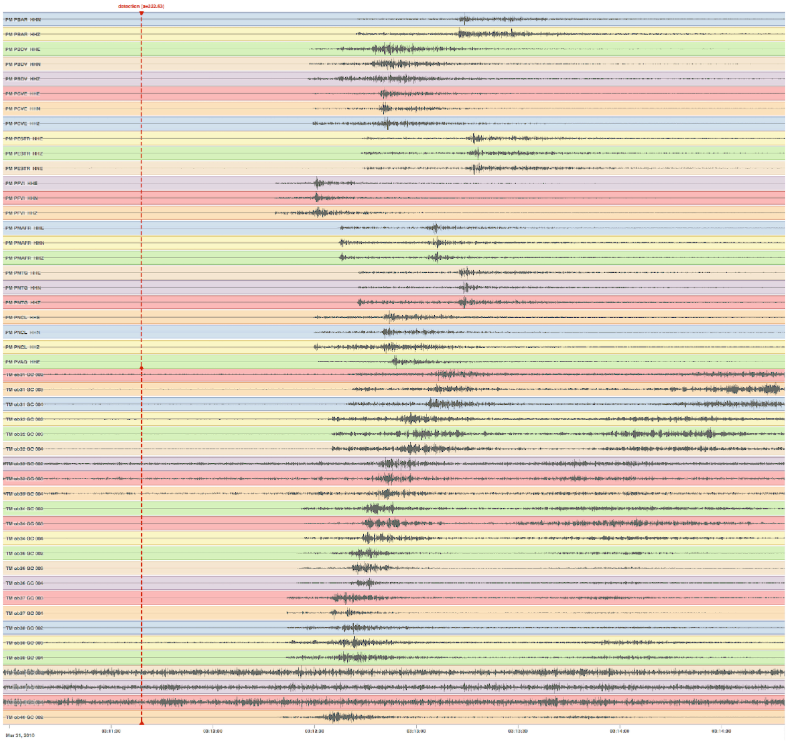

Figure 3.3: Example of an earthquake: detection with value of 322.53, at 03:11:39.000 of 2010-03-31. Data filtered between 5 and 15 Hz.

Figure 3.4: Example of a false positive: detection with value of 156.247 in a change of day, from July 4 to July 5, at 23:58:45.000. The merge of data from these two days around 00:00, generates a signal with high amplitude.

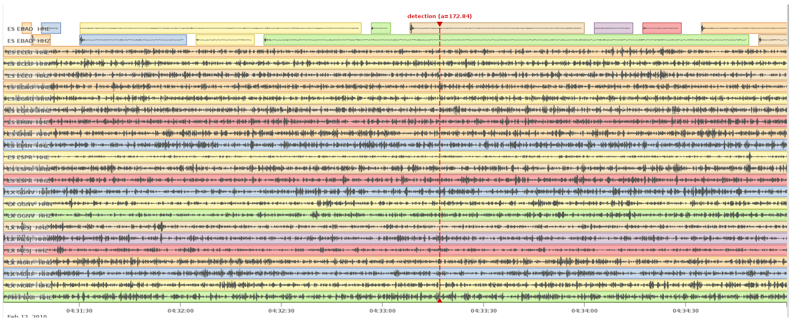

Figure 3.5: Example of a false positive: detection value of 172.84, at 04:33:17 of 2010-02-12, due to lack of data (white spaces). When we have data again, the first signal has a very strong signature with high amplitude.

Figure 3.6 shows the results of manual validation: as can be seen in (a), the number of false positives decreases rapidly above 100.0. We set the threshold for the detections to 110.0, as this value seems a good compromise between detecting earthquakes and avoiding a large number of false positives.

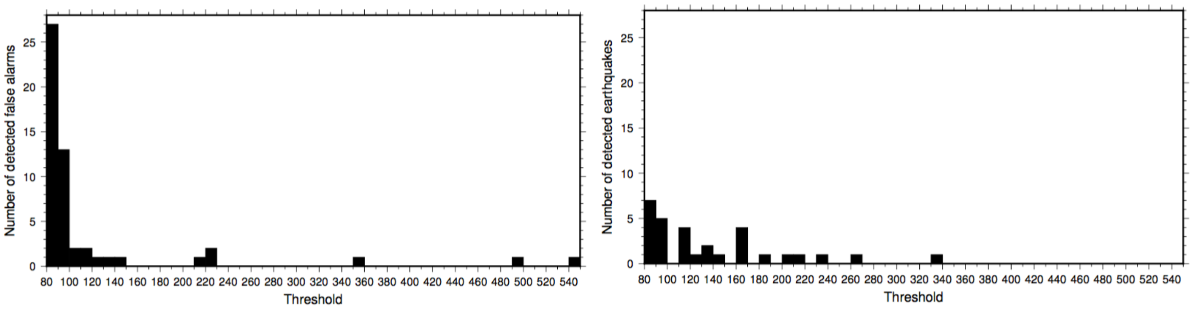

(a) (b)

Figure 3.6: Number of detections versus threshold, for (a) false positives and (b) earthquakes. A threshold of 110.0 is a good compromise between detecting earthquakes and avoiding a large number of false positives.

We used a threshold of 110.0 to scan all the dataset. The detections that fell inside the study area were again manually validated with Snuffler and we found 134 false positives and 153 earthquakes, recorded in land and offshore stations. From these, 112 could be validated using waveforms from OBS stations only.

4 Locations of earthquakes

Automated locations for the 153 detections were computed using LOKI (Grigoli et al., 2013), and verified with NonLinLoc (Lomax et al., 2000), using different velocity models.

4.1 Preparing the waveforms for LOKI

The location process using LOKI is faster if only waveforms with high signal-to-noise ratio are used (e.g. Bormann, 2014). As LOKI might locate coherent noise instead of an earthquake, we decided to adjust the time window of each event according the duration of the earthquake, i.e., without a lot of minutes of record before P wave and/or long coda records. In order to do this, we re-analysed each earthquake in Snuffler, where we manually removed the waveforms of noisy stations, and cut a short time window around the event.

Figure 4.1 shows the number of times that data from each station was used to locate earthquakes: if 0 (black) it means that was a very noisy station and then it was never used for locations; if 153 (white) it means that was a very good station, and its data was always used for the locations of all earthquakes.

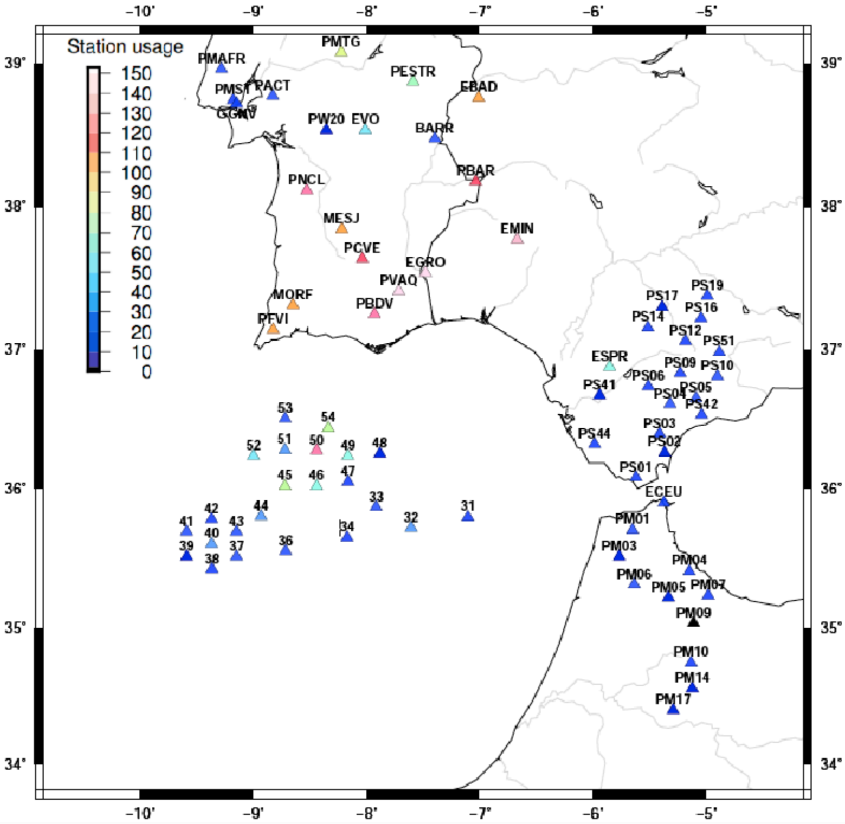

Figure 4.1: Data from each station used to locate earthquakes, using LOKI. This determination was based on visual analysis to the waveforms of each event: 0 (black) cannot locate, 153 (white) can locate all the earthquakes.

We can expect few contributions from the OBS stations, as only six have the potential to contribute above 40 times. The low signal-to-noise ratio of the OBS data might be explained by the fact that most of the stations were located in the accretionary wedge, a sedimentary zone, supporting that thicker sediments provide higher attenuation (Grevemeyer et al., 2016). It could also mean that the OBS might not be well coupled to the ground during acquisition (Dr. Carlos Corela from Instituto Dom Luiz, Lisboa, *personal conversation*).

The stations of the XB network also have a low potential to contribute. This might be explained simply because these stations are far away from the region of interest. Also it could be by the fact that this is a temporary network, and therefore the quality of the data may be low due to installation issues.

Once prepared, the data can be located using LOKI.

4.2 LOKI

LOKI – LOcation of seismic events trough traveltime stacKIng (Grigoli et al., 2013) is a method that uses Python and Obspy libraries, in order to locate seismic events. This method does not require phase picking, which is useful when we have to work with a large amount of data. Also has the advantage of dealing well with local earthquakes, when sometimes the P coda overlaps the S wave and makes difficult to pick the last one.

In spite of its advantages, LOKI has two main disadvantages: it only works with seismic data from three-component stations, therefore, the data from OBS 37, 40, 44, 45 and 46 cannot be used because they lack at least one component (Figure 2.2). Also this method is computationally intensive and cannot work with a huge grid, such as the area used in Lassie. Therefore, we used one of 520 km × 370 km × 80 km from point $11.0°$W, $35.0°$N (Figure 4.2).

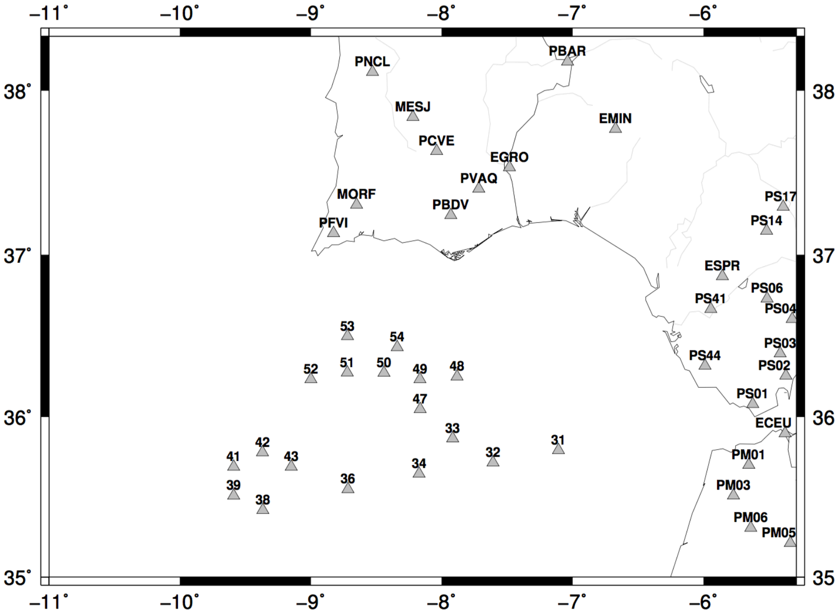

Figure 4.2: 2D projection of the used grid of 520 km × 370 km × 80 km, from point $11.0°$W, $35.0°$N, and three-component seismic stations (grey triangles) from which data can be used in LOKI.

We computed the theoretical arrival times of P and S waves from each node of the grid to all stations with Vel2Grid and Grid2Time programs of NonLinLoc (Lomax et al., 2000), using two different velocity models: the 1D model from Geissler et al. (2010), and the 3D model adapted from Arroucau and Custódio (2015) (Appendix C).

In order to locate the earthquakes, LOKI uses STA/LTA traces, computed from two different characteristic functions: one sensitive to P wave, which is defined as the energy of the vertical component of the seismic trace, and other sensitive to S wave, which is defined using both horizontal component traces. Then LOKI stacks these STA/LTA traces along the theoretical arrival times of P and S waves, for all nodes of the spatial grid, and creates a coherence matrix. This matrix is bounded at 0 (no coherence) and at 1 (perfect coherence). The location is then obtained in the grid point where the matrix has its maximum. To estimate location uncertainties, LOKI relocates the same event five times, perturbing the length of short-time window randomly between 5 and 35 seconds, and calculating the length of long-time window keeping STA/LTA $= 3$.

4.2.1 LOKI results: comparison between 1D and 3D velocity models

All the 153 earthquakes detected by Lassie were located with LOKI, using each station many times as possible (Figure 4.1). We analysed the maximum coherence values obtained with two velocity models (Figure 4.3), as well as the maximum error in hypocentre location (Figure 4.4).

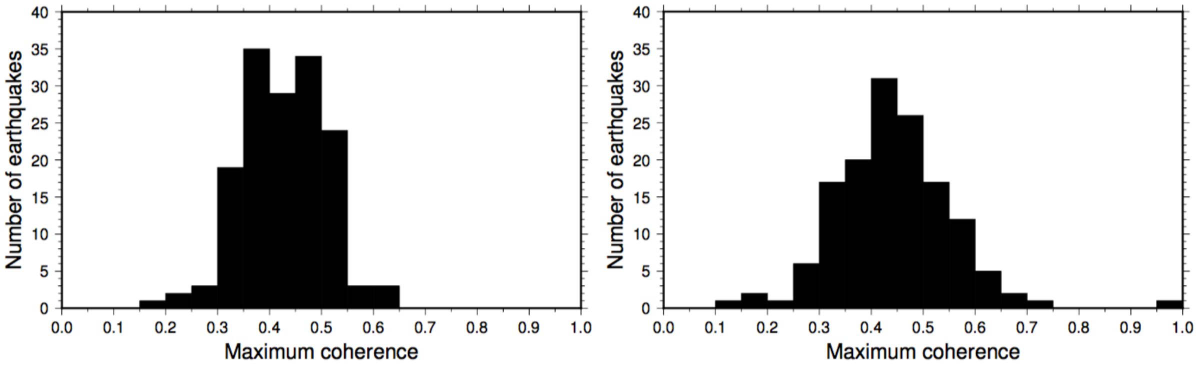

Figure 4.3: Values of maximum coherence for events located with LOKI, with 1D velocity model (left) and 3D velocity model (right). With the last one, higher values of coherence can be reached.

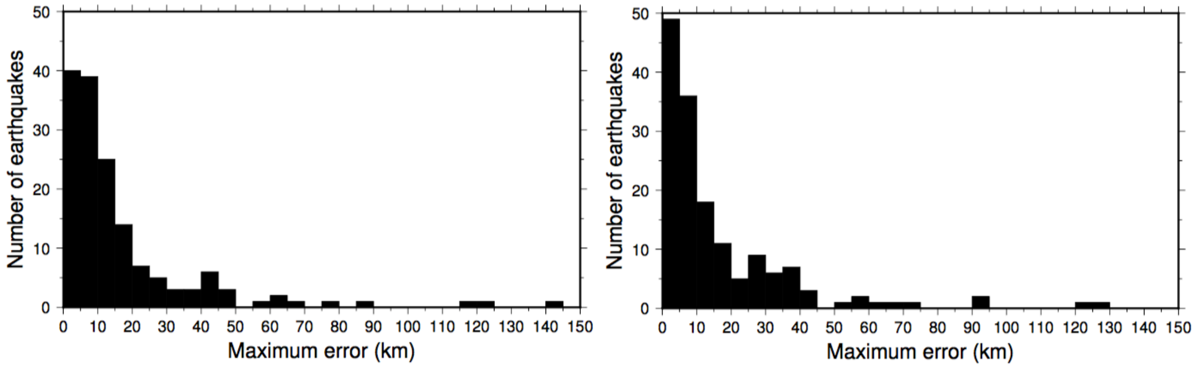

Figure 4.4: Values of maximum hypocentre error for events located with LOKI, with 1D velocity model (left) and 3D velocity model (right). With the last one, we have more earthquakes with lower erros.

As we can see in Figure 4.3, higher values of maximum coherence are reached with 3D model, and by Figure 4.4 we see that the hypocentre errors are minimized with 3D model.

After this analysis and in both models, we dismissed all the events with maximum coherence lower than 0.4 or/and maximum hypocentre errors higher than 10 km. Inside study region we found 42 earthquakes with 1D model, and 54 with 3D model (Figure 4.5). It is noted that some of the earthquakes are located outside the study area, while with Lassie they were inside.

Both models have in common 30 earthquakes, and the distance between their epicentres and difference of depths can be seen in Figure 4.6. Comparing the common earthquakes, in general the epicentres are located more to south with the 3D model, and the differences between them are small, only with two cases reaching values higher than 17 km. The differences between depths obtained for the same events reach about 43 km. With the 3D velocity model we also can see deep seismicity at about 60 km.

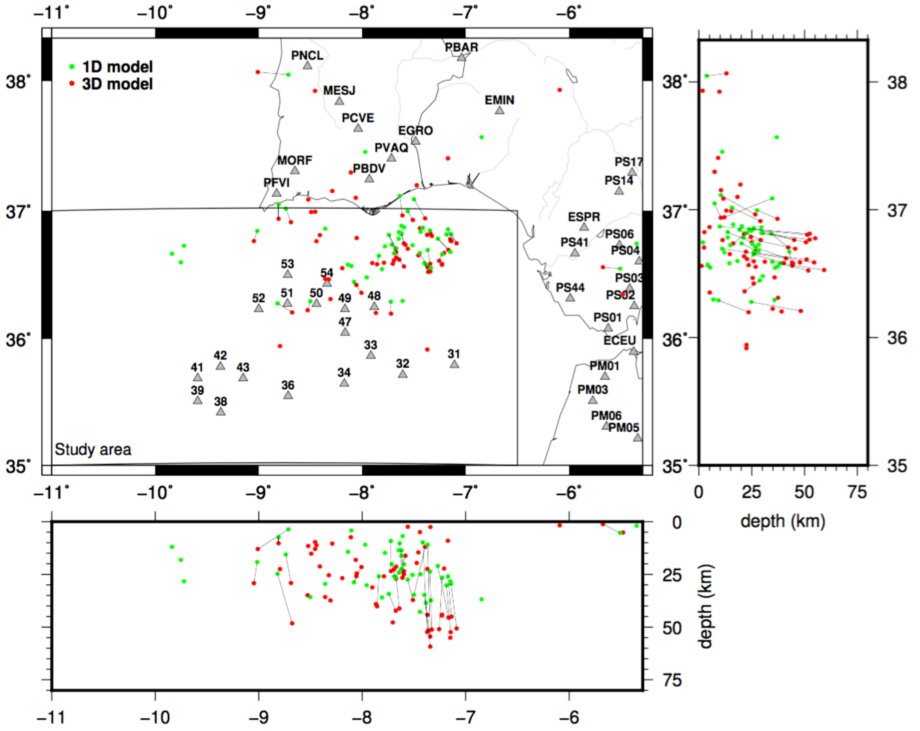

Figure 4.5: Map with the locations of the earthquakes with 1D velocity model (green dots) and 3D velocity model (red dots), with LOKI. Earthquakes with the same origin time are linked.

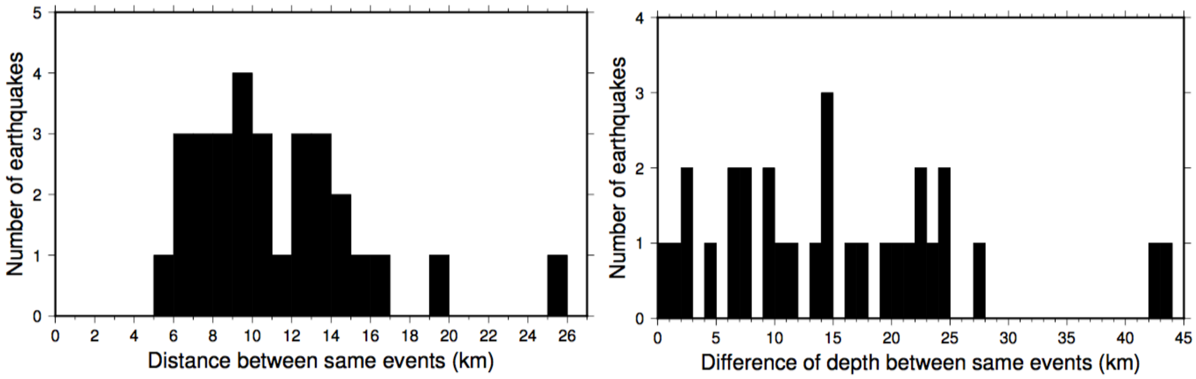

Figure 4.6: Distribution of distance between same events (left) and difference of depth for same events (right), located with LOKI with 1D and 3D velocity models.

Figures 4.3 and 4.4 indicate that the 3D velocity model leads to smaller error in earthquake locations. To confirm this, we performed a visual inspection to the results of the coherence matrices and randomly selected two examples to show here (Figures 4.7 and 4.8). The inspection shows that the 3D velocity model does in fact result in more robust hypocentre locations because it produces higher values of maximum coherence compared with 1D.

For each earthquake, we also quantified the area with a coherence value higher than 95% of maximum coherence. We then summed all the areas and for locations with 1D model we have 66809 km^2, and with 3D model we have only 43851 km^2, a much lower area.

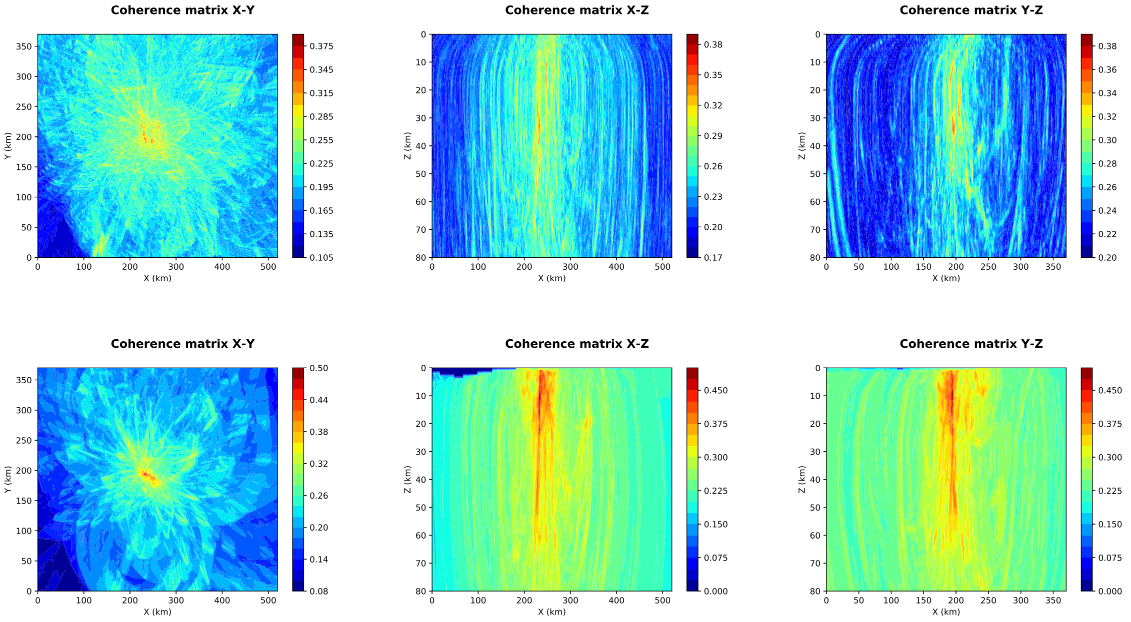

Figure 4.7: Location of the earthquake occurred on 2010-02-28 at 16:32:49, using LOKI with 1D (above) and 3D (below) velocity models. From left to right we see cross sections of the coherence matrix in X-Y, X-Z and Y-Z plans. It is clear that 3D velocity model provides more accurate locations.

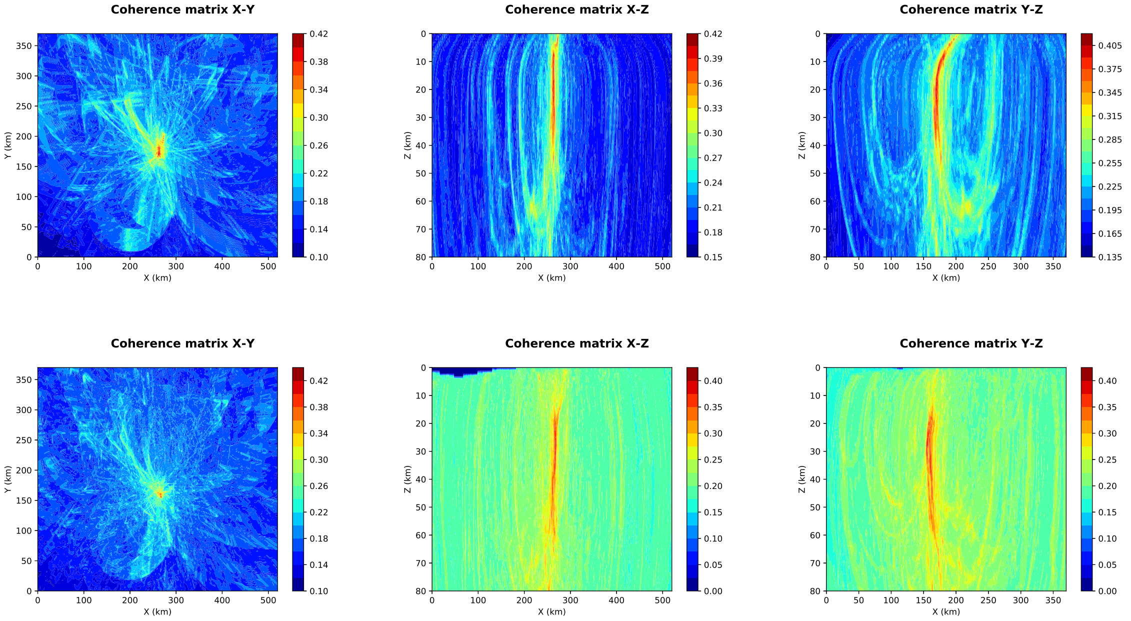

Figure 4.8: Location of the earthquake occurred on 2010-03-21 at 05:27:10, using LOKI 1D (above) and 3D (below) velocity models. From left to right we see cross sections of the coherence matrix in X-Y, X-Z and Y-Z plans. It is clear that 3D velocity model provides more accurate locations.

The 3D velocity model seems to be better suited for earthquake locations in this region. LOKI provides only the maximum error of hypocentre estimation, which result from the bootstrap analysis. In order to quantify the location errors in terms of RMS, GAP and length of the semi-major axis of the ellipse, we have to use a different method, such as NonLinLoc.

4.3 NonLinLoc

NonLinLoc – Non-Linear Location (Lomax et al., 2000) consists on a set of several programs that can create velocity grids from a velocity model chosen by the user, calculate theoretical travel times of seismic waves from each point of a defined grid to all stations, and estimate the location of seismic events. A great advantage of NonLinLoc is that it uses non-linear techniques to locate earthquakes.

In this work we used three programs from NonLinLoc, all in the Non-Global mode, i.e., considering a plan shape Earth, locally as a rectangle with a (x, y, z, t) coordinate system. These programs were:

- Vel2Grid: with this program we used the 3D velocity model to create a slowness grid of $581 \times 571 \times 81$ points, equally spaced from 1.0 km, starting from point $11.0°$W, $34.0°$N (Figure 4.9).

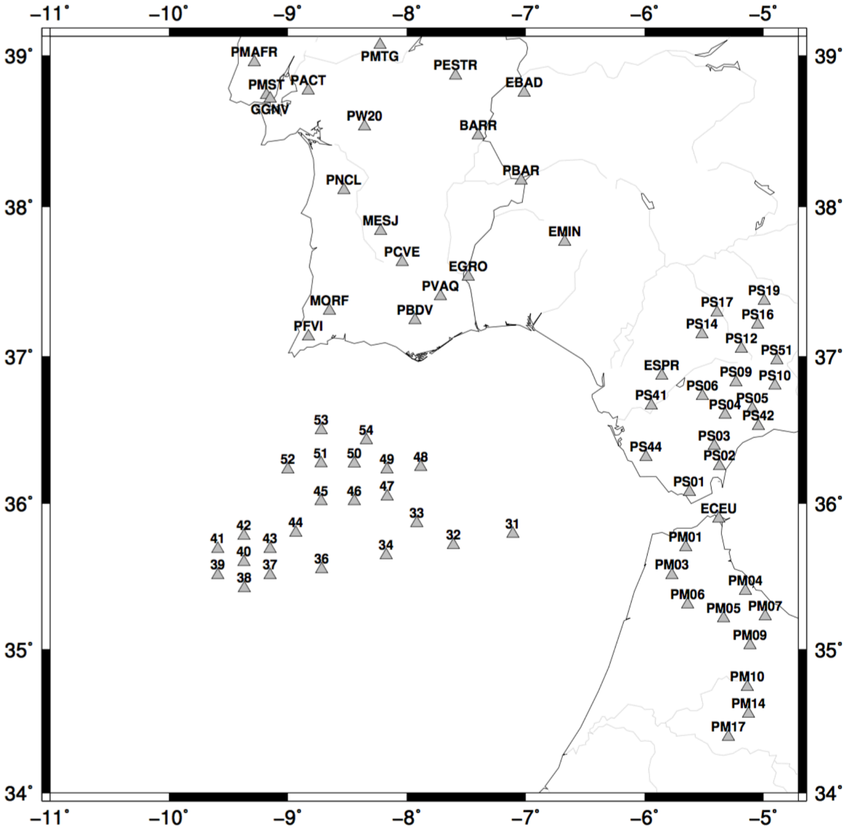

Figure 4.9: 2D projection of the used grid of $580 \times 570 \times 80$ km from point $11.0°$W, $34.0°$N, and seismic stations (grey triangles) used in NonLinLoc.

- Grid2Time: using the grid created above, for each event the program calculates theoretical travel times of P and S waves between each station and all nodes, and saves them to binary files. This way, the travel times are calculated only once, which make the next program more efficient.

- NLLoc: before using this, we had to use Snuffler to manually pick P and S waves. We then transformed the resulting phase catalogue to the NLLOC_OBS format, and passed it to NLLoc program. In this, it uses the Oct-Tree Importance Sampling Algorithm, which uses a geometry of oct-tree division of rectangular cells. In each cell the algorithm estimates the probability density function (PDF) for hypocenter location. In each interaction, the cell with large PDF value is divided in 8 cells, and the process begins again. Once the minimum cell size is reached, the algorithm stops searching. This method converges rapidly and is user friendly, as it only needs the grid size and the number of nodes to process.

Despite the advantages, using NonLinLoc to locate earthquakes requires phase picking and identification, which is a time consuming task.

4.3.1 NonLinLoc results with 3D velocity model

The 153 earthquakes provided by Lassie and pre-processed in Section 4.1, were located using the 3D velocity model from Arroucau and Custódio (2015). Then the RMS and GAP values were analysed (Figure 4.10), as well as the length of the semi-major axis and error in depth (Figure 4.11).

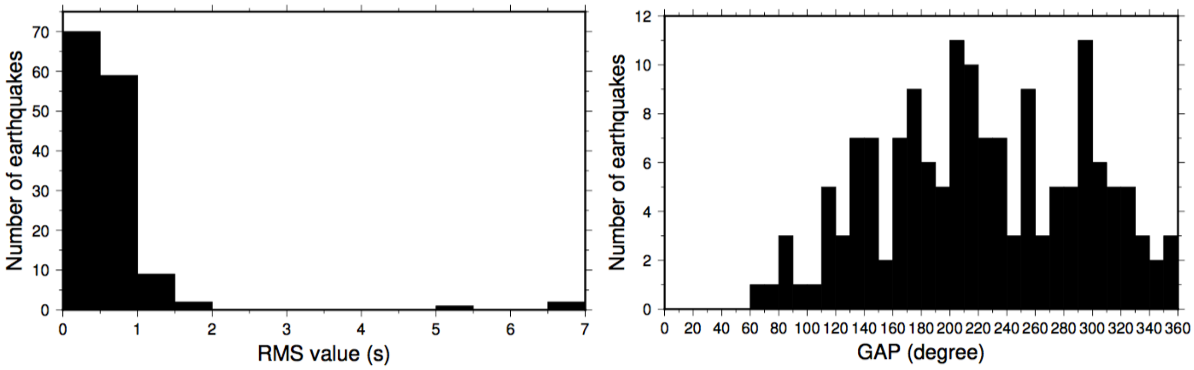

Figure 4.10: Distribution of RMS values (left) and GAP (right), of the 153 earthquakes located with NonLinLoc - 3D model. For convenience of visualization, from RMS histogram we removed ten outliers, varing between 12.3328 and 436.366 seconds.

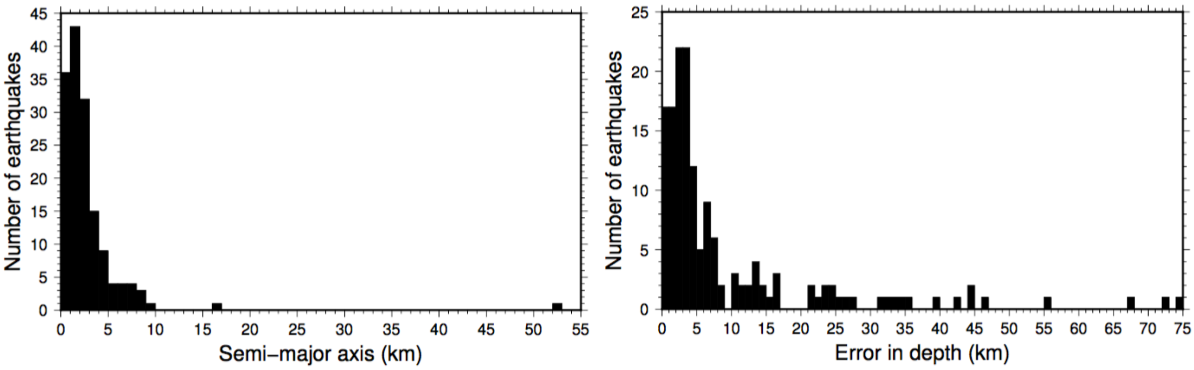

Figure 4.11: Distribution of errors of the 153 earthquakes located with NonLinLoc - 3D model: length of semi-major axis of the epicentre location (left) and error in depth (right).

From the 153 earthquakes, we only located 61 inside the study region with RMS lower than or equal to 1.0 s, semi-major axis lower than or equal to 10 km, and GAP lower than or equal to 220°. Typically, a well constrained location has a GAP value of less than 180° (e.g. Husen and Hardebeck, 2010), but since only a small number of OBS stations had the potential to be used (Figure 4.1), it was decided to choose 220°. In Figure 4.12 we have the map with the locations obtained, as well as the number of times that each station was used to pick phases.

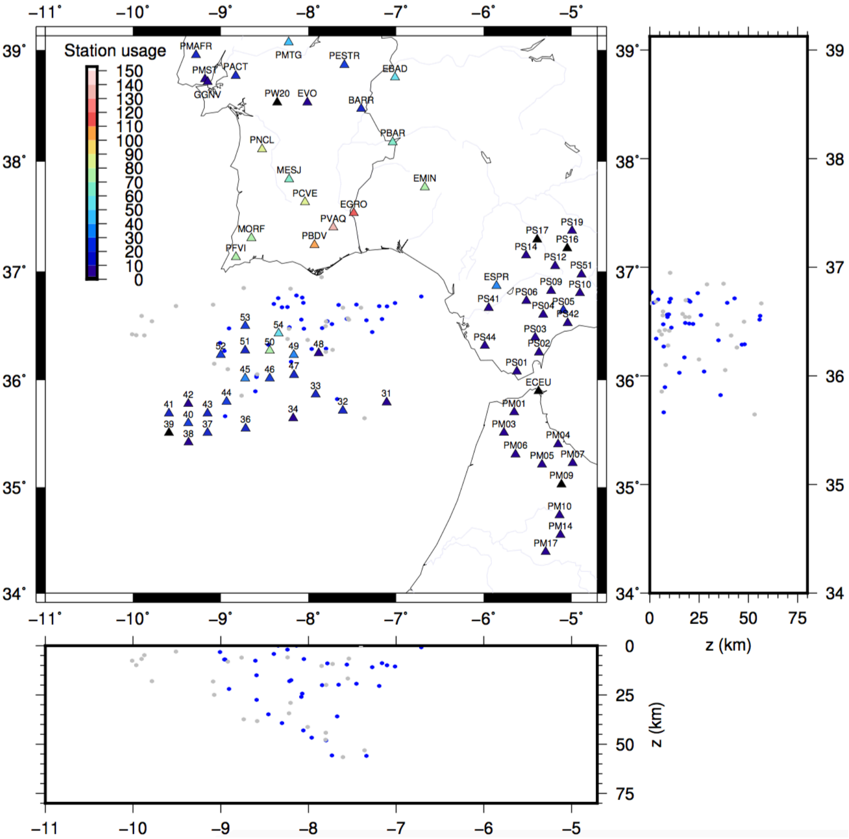

Figure 4.12: Colour coded locations inside the study region, obtained with a 3D velocity model in NonLinLoc: all the earthquakes (dots) have RMS $\leq$ 1.0 s and a length of semi-major axis $\leq$ 10 km. Grey dots represent earthquakes with $180^\circ <$ GAP $\leq 220^\circ$, and the blue dots represent the ones with GAP $\leq 180^\circ$. The seismic stations are also colour coded by the number of times that each one was used to locate an earthquake.

The distribution of earthquakes shows moderate depth seismicity, until around 60 km depth. Due to low number of earthquakes, we cannot infer if there are any clusters of events, therefore this analysis is done with waveform similarity (Section 5).

In the next two Subsections these results are compared with the ones obtained by Grevemeyer et al. (2016) and IPMA.

4.3.2 Comparison between NonLinLoc with 3D velocity model and Grevemeyer et al. (2016) study

As already mentioned, Grevemeyer et al. (2016) also studied the gulf of Cadiz using a similar dataset. In their study they used phase picking and identification to perform the locations, and found 51 earthquakes with RMS lower than 1.3 s, inside our study area and at the same time.

Comparing our catalogue with theirs, there are 26 earthquakes with the same origin time (Figure 4.13). The epicentres are quite similar, with only four pairs of epicentres distanced from more than 15 km (Figure 4.14 left). In terms of depth (Figure 4.14 right), our study usually brings the earthquakes closer to the surface (Figure 4.13) and the differences can reach around 61 km. Both methods required the time consuming task of phase picking and identification, but using a 3D velocity model led us to obtain 61 earthquakes with lower RMS values, 10 more than those located.

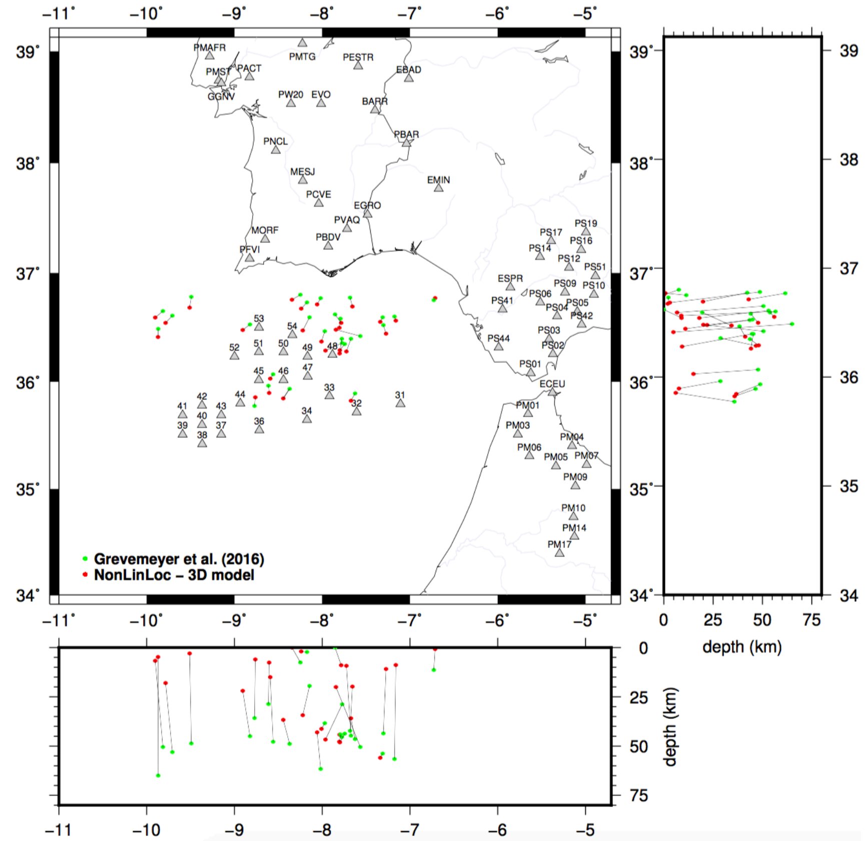

Figure 4.13: Locations of the 26 common earthquakes in the catalogues obtained by Grevemeyer et al. (2016) (green dots) and by NonLinLoc - 3D model (red dots). Earthquakes with the same origin time are linked.

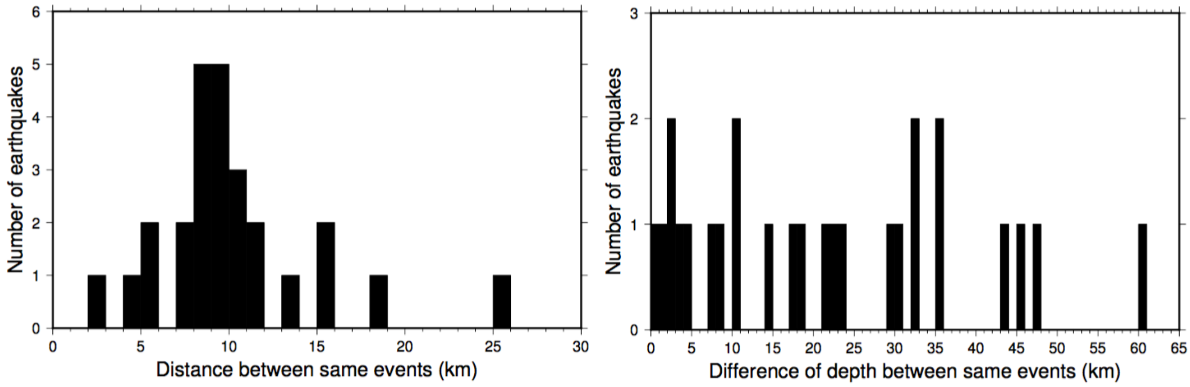

Figure 4.14: Comparison between 26 common earthquakes in the catalogues obtained by NonLinLoc - 3D model and Grevemeyer et al. (2016): distribution of distance between same epicentres (left) and differences of depth of same events (right).

4.3.3 Comparison between NonLinLoc with 3D velocity model and IPMA results

The methodology used by IPMA to locate earthquakes is also phase picking and identification of seismic phases, using only land stations. Their catalogue reported only 18 earthquakes with RMS lower than 1.0 s and GAP lower than 220°.

In order to show the differences between the locations with NonLinLoc using the 3D model and locations reported by IPMA, we compared the catalogues to see which earthquakes had the same origin time. The catalogues have in common 58 earthquakes (Figure 4.15). In terms of epicentres, they are quite similar, but our study tends to locate them further southwest. IPMA's depths are located around 10-30 km, while the locations obtained with NonLinLoc and 3D model tend to be either lower or higher.

From these 58 earthquakes in common, only 13 reported by IPMA have RMS lower than 1.0 s and GAP lower to 220°. It is clear that using a 3D velocity model and OBS stations improves the location of the earthquakes.

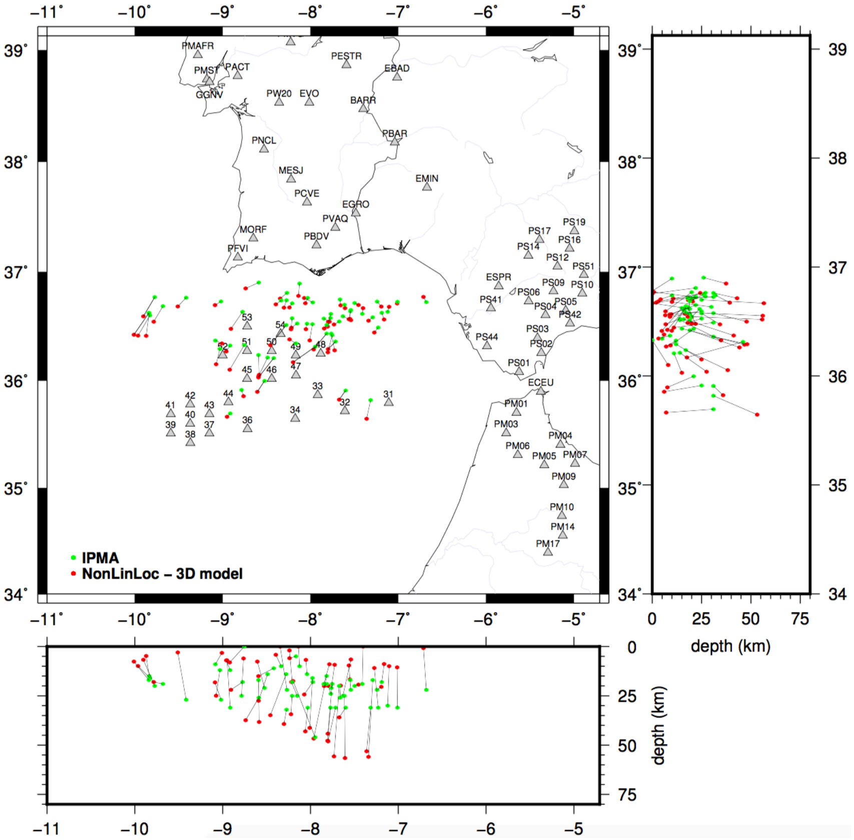

Figure 4.15: Locations of the 58 common earthquakes in the catalogues obtained by NonLinLoc - 3D model (red dots) and IPMA (green dots). Earthquakes with the same origin time are linked.

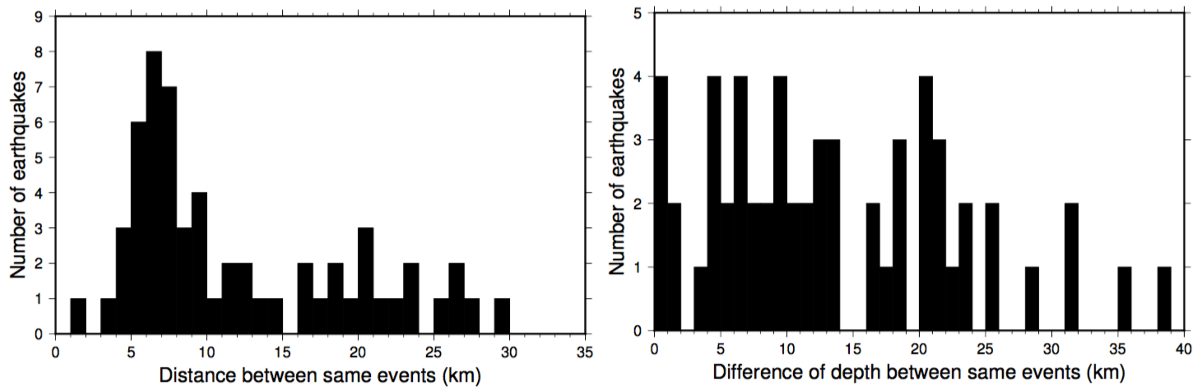

Figure 4.16: Result of the comparison between hypocentre locations obtained with NonLinLoc - 3D model and IPMA: distribution of distance between same epicentres of events (left) and differences of depth of same events (right).

5 Analysing the seismic catalogue: magnitudes and waveform similarity

5.1 Determination of magnitudes

Before estimating the magnitude of earthquakes, we need to remove the instrumental response from the waveforms. In order to do so, we need to know the characteristics of instruments, such as poles, zeros, gain and sensitivity. This information, given for instance by the RESP files or the dataless file, is not available for OBS and some land stations. Therefore, we used only 33 land stations, for which we had this information (Figure 5.2).

After removing the response, we determined the local magnitude (M_L) of the 61 earthquakes located with NonLinLoc - 3D velocity model, using the equation proposed by Carrilho and Vales (2009) for Portugal mainland and adjacent areas:

$$M_L = \log A - 1.287 \log \Delta + 0.00061\Delta - 2.147 + S \tag{5.1}$$

where A is the amplitude (nn), Δ is the hipocentral distance (km) and S is a term for the station correction. The last term, S, was only available for six stations (GGNV, MESJ, MORF, PESTR, PFVI and PVAQ), therefore, for the remaining stations we assumed $S = 0.0$.

The results, presented in Figure 5.1, show that magnitudes are distributed between 0.0 and 4.3. Most of the earthquakes have a small local magnitude, of less than 3.0. Only seven earthquakes have magnitude greater than or equal to 3.0. The colour coded bars help rapidly visualise the map in Figure 5.2, where the earthquake locations are shown, also colour coded according to magnitude.

The largest earthquake occurred during the deployment was a magnitude 4.3, on March, 31, with coordinates 9.90301°W, 36.5928°N.

The earthquakes with higher magnitudes are found at depths of around 40 km. The ones with magnitudes between 2.0 and 3.0 can be found deeper, until around 60 km.

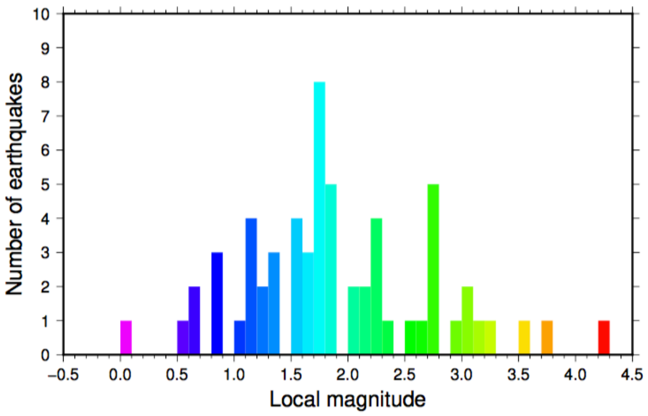

Figure 5.1: Distribution of local magnitudes of the 61 earthquakes located with NonLinLoc - 3D model, colour coded to help rapidly visualise the map in Figure 5.2.

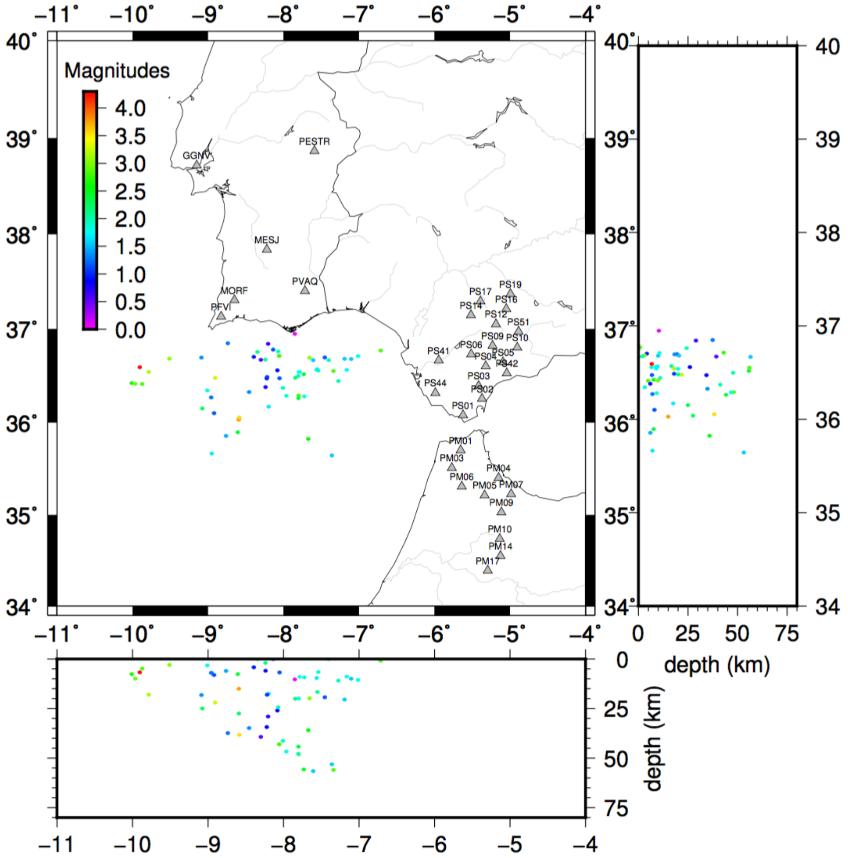

Figure 5.2: Map with stations used for estimation of magnitudes, and earthquakes colour coded according to magnitude.

5.2 Cross-correlation of waveforms

In order to verify if the waveforms share the same source mechanisms (focal mechanism and radiation pattern) and site effects, meaning that these belong to the same tectonic structure (e.g. Barani et al., 2007 and Akuhara and Mochizuki, 2014), we cross-correlated waveforms of each two events. As the propagation paths of the phases must be similar, the cross-correlation is done only between earthquakes recorded at the same station.

We cross-correlate pairs of waveforms, using only the Z components of each event, around the P wave, starting 0.6 seconds before it and end 1.0 seconds after this. Figure 5.3 shows the result of this analysis. Most of the events have cross-correlation coefficients below 0.8. We found 23 cross-correlations between waveforms with value greater than or equal to 0.8. Two examples of this can be seen in Figures 5.4 and 5.5, determined for stations ESPR and OBS 40, respectively.

After this, we used Python/Obspy libraries to search for clusters of events. Although we were using a small number of events, only 61 earthquakes, the analysis of clusters provided positive results: considering a cluster a set of at least four events with cross-correlation coefficients between waveforms greater than or equal to 0.8, we obtained two clusters of events, one recorded by ESPR (Figure 5.6) and other by PBDV (Figure 5.7).

In the cluster recorded by ESPR station is one earthquake occurred on March, 24 (magnitude 2.8), the largest earthquake occurred during the deployment, on March, 31 (magnitude 4.3), and two occurred on May, 29 (magnitudes 2.6 and 2.9). In the cluster recorded by PBDV station is one earthquake occurred on January, 24 (magnitude 3.0), one on March, 20 (magnitude 1.6), one on March, 27 (magnitude 1.8), and one on May, 31 (magnitude 1.5).

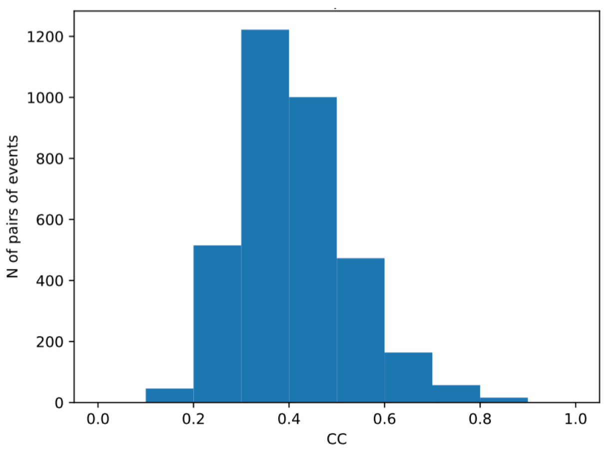

Figure 5.3: Histogram resulted from the cross-correlation analysis. CC stands for cross-correlation coefficient.

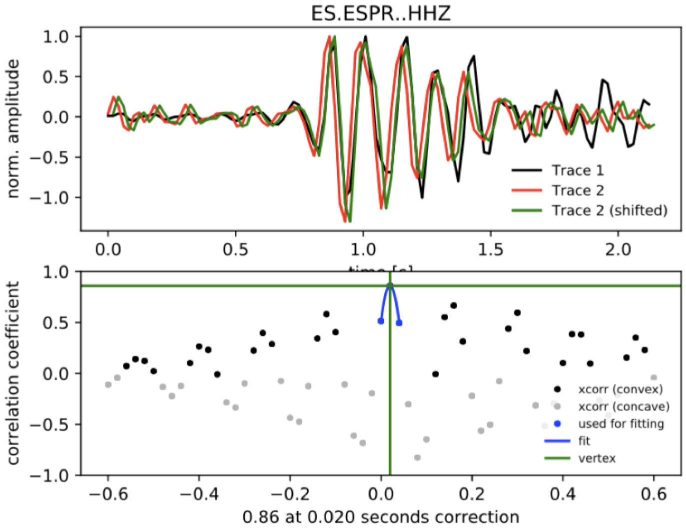

Figure 5.4: Example of a cross-correlation coefficient of 0.86 in station ESPR, for the pair of events occurred on 2010-03-24T21:23:20 (9.871°W, 36.413°N) and 2010-07-04T18:15:04 (7.193°W, 36.683°N).

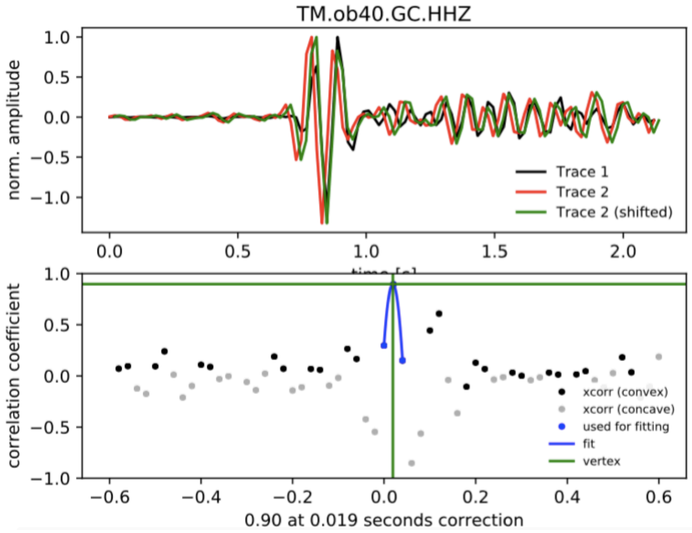

Figure 5.5: Example of a cross-correlation coefficient of 0.90 in OBS 40, for the pair of events occurred on 2010-02-06T22:00:07 (8.591°W, 36.040°N) and 2010-06-01T10:46:30 (7.844°W, 36.481°N).

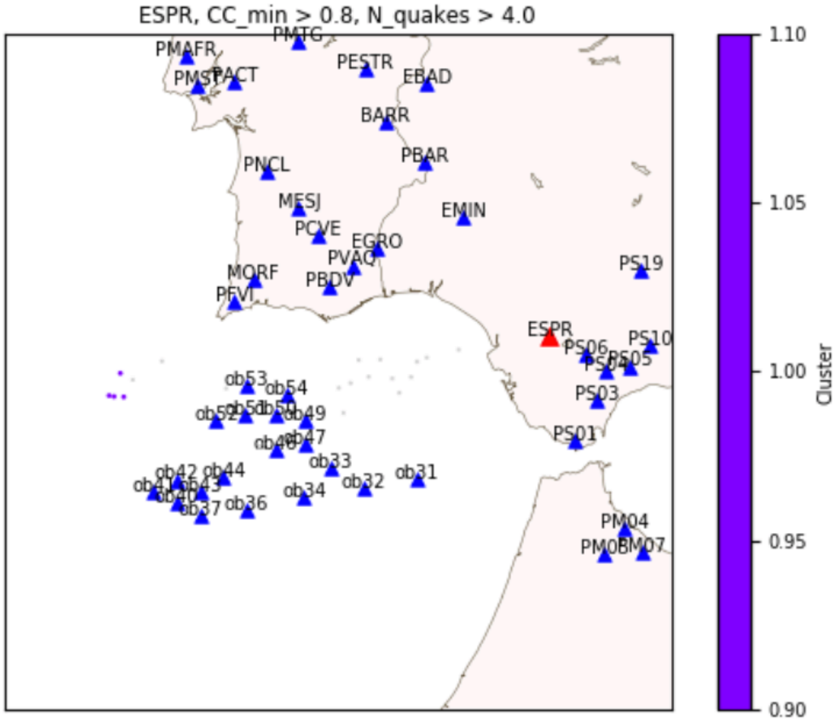

Figure 5.6: Map with a cluster of events (purple dots) detected by station ESPR (red triangle) with NonLinLoc - 3D model. Grey dots are the other locations made by this station.

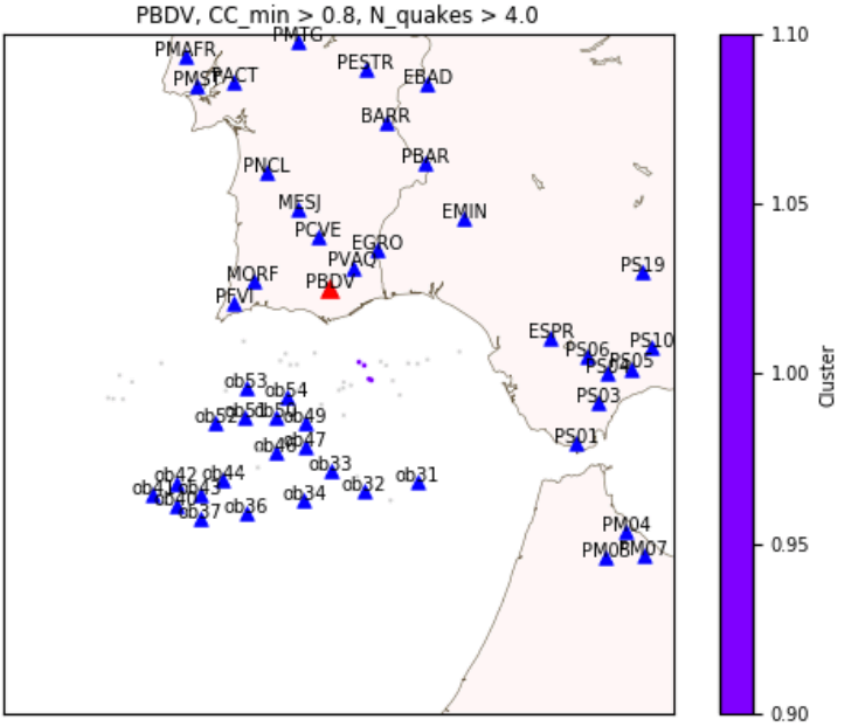

Figure 5.7: Map with a cluster of events (purple dots) detected by station PBDV (red triangle), with NonLinLoc - 3D model. Grey dots are the other locations made by this station.

These events were plotted in a map of faults (Figure 5.8). As can be seen, the cluster identified by station ESPR is near a set of faults, but not explicitly above one. The cluster identified by station PBDV is far from any fault. To get more conclusions about these clusters, it is necessary to perform the same analysis on an enlarged dataset.

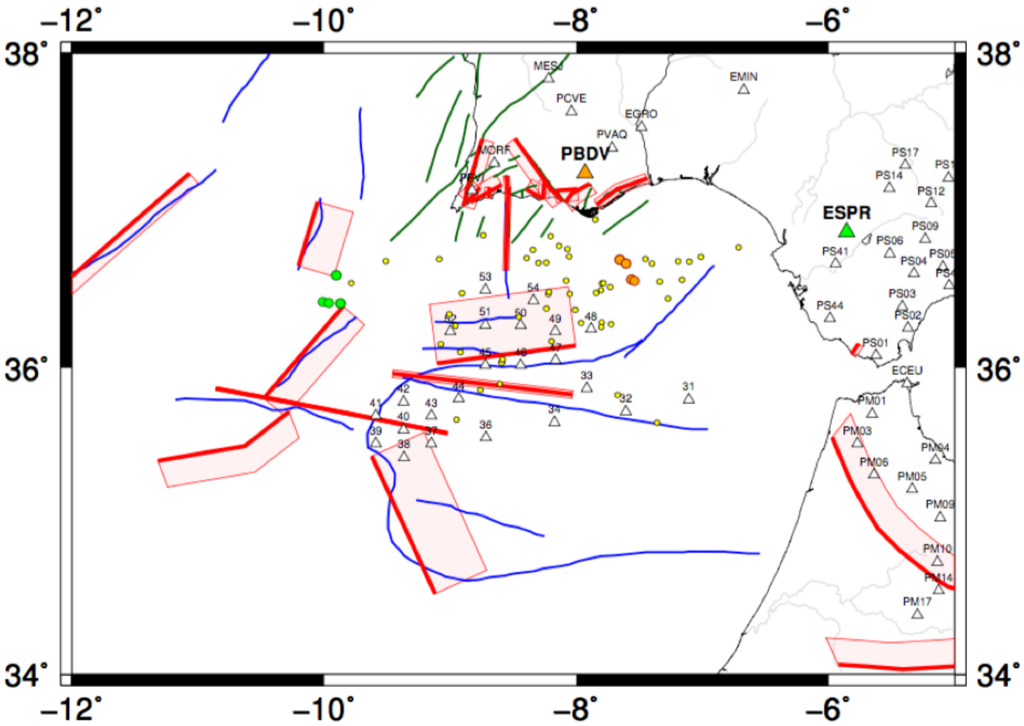

Figure 5.8: Map of geologically mapped faults and the two clusters detected by stations ESPR (green dots) and PBDV (orange dots). Yellow dots represent the other earthquakes located with NonLinLoc - 3D model, that do not belong to any cluster.

6 Conclusion

In this work we proposed to use a new methodology to study a particular area in gulf of Cadiz, from 11.0°W to 6.5°W and 35.0°N to 37.0°N, from January, 20 to July, 21 of 2010, using data from OBS and several land stations (Figure 2.1).

Lassie is an effective method to detect earthquakes. It is computationally fast and can work with high volumes of data: for our six months of data, Lassie only needed one night to scan all dataset. This method provided a good number of events, that had to be manually validated in order to determine if each detection was in fact an earthquake or a false alarm. After the analysis to 10% of data, we determined that the detection threshold of 110.0 was a good compromise between having a good number of earthquakes and avoiding a large number of false positives (Figure 3.6). For all dataset, Lassie detected 153 earthquakes inside the study area.

Automated locations for these detections were computed using LOKI (Grigoli et al., 2013), and verified with NonLinLoc (Lomax et al., 2000), using different velocity models. In order to optimize the location process, before the locations we manually removed the stations with bad signal-to-noise ratio, and adjusted a short time window for each event. We cannot expect a great contribution from the OBS stations, which are very noisy (Figure 4.1). As most of these are located in a sedimentary area, the noise could be the result of poor coupling to the seafloor. Also, the stations of XB network have low contributions, and the reason could be the distance to the study area or installation issues.

We started by using LOKI, a method based on STA/LTA traces and a coherence matrix. This method does not require the demanding task of phase picking and identification. In the other hand, it might be subject to locate false alarms, such as local events, as it is very sensitive to coherent noise. Nevertheless, the analysis to 1D and 3D velocity models' results allowed us to confirm that the last one can provide more robust locations. This was confirmed not only by visual inspection to the coherence matrices (Figures 4.7 and 4.8), but also by the coherence values themselves. With 3D model we obtained higher values of maximum coherence (Figure 4.3). The area occupied by nodes with coherence values greater than 95% of maximum coherence, for the overall locations, is 66809 km^2 for 1D model, and only 43851 km^2 for the 3D model.

NonLinLoc adopts a methodology that requires more effort, since we need to pick and identify the seismic phases. It is based on posterior probabilistic density functions, and it is more useful than LOKI if we want to quantify the errors. We used the 3D velocity model and obtained 61 earthquakes with RMS lower than or equal to 1.0 seconds, GAP lower than or equal to 220°, and maximum length of the semi-major axis below 10 km (Figures 4.10, 4.11 and 4.12). Ideally, the OBS should minimize the GAP, but since these stations are very noisy, sometimes it was very difficult to distinguish between noise and P or S arrivals, and the pickings were not done in the waveforms of these stations.

The locations obtained with NonLinLoc - 3D model were compared with the ones reported by Grevemeyer et al. (2016). The catalogues have 26 earthquakes in common, with distance between same events reaching around 26 km, and differences of depth reaching around 61 km (Figures 4.13 and 4.14). Our study located 10 more earthquakes with lower RMS values, showing that using 3D velocity model results in more robust hypocentres.

We also compared the locations using NonLinLoc - 3D model with the locations reported by IPMA. They only got 18 earthquakes with the condition of RMS equal to or lower than 1.0 seconds, and a GAP equal to or lower than 220°. This low value is expectable since IPMA do not use OBS stations. The catalogues have in common 58 earthquakes (Figure 4.15), with differences between epicentres reaching around 30 km, and differences of depth reaching around 39 km (Figure 4.16). From these 58 in common, only 13 earthquakes reported by IPMA had RMS equal to or lower than 1.0 seconds, and a GAP equal to or lower than 220°, which shows that using the 3D velocity model and OBS stations allow us to obtain more robust hypocentres.

Independently of the process used, LOKI or NonLinLoc, both studies show moderate-depth seismicity, until around 60 km (Figures 4.5 and 4.12). These depths are also reported by Stich et al. (2005). Furthermore, both studies do not show seismic activity near the OBS 37 – 43, which are on top of one SWIM fault, but there is activity in other SWIM fault, since we located earthquakes near OBS 32 and 44.

With NonLinLoc - 3D velocity model we located only two earthquakes in the thickest part of the accretionary wedge, below around 36.0°N. Grevemeyer et al. (2016) also reported this lack of seismicity in this area, which can be explained by the fact that thicker sediments provide higher attenuation.

The estimated local magnitudes are in a range between 0.0 and 4.3 (Figure 5.1). The earthquakes with higher magnitudes are found at around 25 km depths, and the ones with magnitudes between 2.0 and 3.0 can be found deeper, until around 60 km (Figure 5.2). As we did not have the instrument response files for all stations, we could not use OBS and some land stations for magnitude estimation.

Regarding the analysis of waveform similarity, because the number of located earthquakes is low, we only identified two clusters with four events each, with cross-correlation coefficients higher than of equal to 0.8 (Figures 5.6 and 5.7). While one of these clusters is located near a set of faults, the other is far apart from any fault (Figure 5.8). Further studies with larger datasets are needed to better understand the region.

References

Akuhara, T. and Mochizuki, K. Application of cluster analysis based on waveform cross-correlation coefficients to data recorded by ocean-bottom seismometers: results from off the Kii Peninsula. *Earth, Planets and Space*, 66(1):1–13, 2014. doi: 10.1186/1880-5981-66-80.

Arroucau, P. and Custódio, S. A hierarchical bayesian approach for earthquake location and data uncertainty estimation in 3D heterogeneous media. *Geophysical Research Abstracts, 17*, 2015.

Barani, S., Ferretti, G., Massa, M., and Spallarossa, D. The waveform similarity approach to identify dependent events in instrumental seismic catalogues. *Geophysical Journal International*, 168:100–108, 2007. doi: 10.1111/j.1365-246X.2006.03207.x.

Beyreuther, M., Barsch, R., Krischer, L., Megies, T., Behr, Y., and Wassermann, J. Obspy: A python toolbox for seismology. *SRL*, 81(3):530–533, 2010. doi:10.1785/gssrl.81.3.530.

Bormann, P. *Seismic Noise*, pages 1–27. Springer Berlin Heidelberg, 2014. ISBN 978-3-642-36197-5. doi: 10.1007/978-3-642-36197-5_289-1.

Carrilho, F. and Vales, D. Calibration of magnitude M_L for Portugal mainland and adjacent areas. *6th Symposium of the Portuguese Association of Meteorology*, 2009.

DeMets, C., Gordon, R. G., and Argus, D. F. Geologically current plate motions. *Geophysical Journal International*, 181(1):1–80, 2010. doi: 10.1111/j.1365-246X.2009.04491.x.

Duarte, J., Rosas, F., Terrinha, P., Schellart, W., Boutelier, D., Gutscher, M.-A., and Ribeiro, A. Are subduction zones invading the Atlantic? Evidence from the southwest Iberia margin. *Geology*, 42(3): 329 –329, 2014. doi: 10.1130/G35420Y.1.

FDSN. International Federation of Digital Seismograph Networks. http://www.fdsn.org/.

Geissler, W. H., Matias, L., Stich, D., Carrilho, F., Jokat, W., Monna, S., IbenBrahim, A., Mancilla, F., Gutscher, M.-A., Sallarès, V., and Zitellini, N. Focal mechanisms for subcrustal earthquakes in the Gulf of Cadiz from a dense OBS deployment. *Geophys. Res. Lett.*, 37(18):L18309, 2010. doi:10.1029/2010GL044289.

Grevemeyer, I., Matias, L., and Silva, S. Mantle earthquakes beneath the South Iberia continental margin and Gulf of Cadiz - constraints from an onshore-offshore seismological network. *(accepted) Journal of Geodynamics*, 2016. doi:10.1016/j.jog.2016.06.001.

Grevemeyer, I. e. a. FS Poseidon POS389 & POS393 & FS Maria S. Merian MSM15/5: TOPO-MED - Topographic, structural and seismotectonic consequences of plate re-organization in the Gulf of Cadiz and Alboran Sea, POS389: Valletta, Malta – Malaga, Spain, 06.–17.08.2009; POS393: Malaga, Spain – Faro, Portugal, 14.–24.01.2010, MSM15/5: Valletta, Malta - Rostock, Germany, 17.–29.07.2010. *IFM-GEOMAR Report, 45. IFM-GEOMAR, Kiel*, page 41 pp, 2011. doi:10.3289/ifm-geomar_rep_45_2011.

Grigoli, F., Cesca, S., Amoroso, O., Emolo, A., Zollo, A., and Dahm, T. Automated seismic event location by waveform coherence analysis. *Geophysical Journal International*, 2013. doi:10.1093/gji/ggt477.

Hafez, A. G., Khan, T. A., and Kohda, T. Earthquake onset detection using spectro-ratio on multi-threshold time–frequency sub-band. *Digit. Signal Process.*, 19(1):118–126, 2009. doi:10.1016/j.dsp.2008.08.003.

Heimann, S. Snuffler, 2012. http://emolch.github.io/pyrocko/v0.2/index.html.

Heimann, S., Matos, C., Cesca, S., Custódio, S., and Rio, I. Lassie: A versatile tool to detect and locate seismic activity. *(in prep.)*, 2015.

Husen, S. and Hardebeck, J. Earthquake location accuracy. *Community Online Resource for Statistical Seismicity Analysis. Available at `http://www.corssa.org`.*, 2010. doi: 10.5078/corssa-55815573.

IPMA. Instituto Português do Mar e da Atmosfera, i. p. http://www.ipma.pt/pt/.

Lomax, A., Virieux, J., Volant, P., and Berge-Thierry, C. Probabilistic Earthquake Location in 3D and Layered Models. In Thurber, C. H. and Rabinowitz, N., editors, *Advances in Seismic Event Location*, pages 101–134. Springer Netherlands, 2000. ISBN 978-94-015-9536-0. doi:10.1007/978-94-015-9536-0_5.

Podvin, P. and Lecomte, I. Finite difference computation of traveltimes in very contrasted velocity models: a massively parallel approach and its associated tools. *Geophysical Journal International*, 105(1): 271–284, 1991. doi:10.1111/j.1365-246X.1991.tb03461.x.

Ross, Z. and Ben-Zion, Y. An earthquake detection algorithm with pseudo-probabilities of multiple indicators. *Geophysical Journal International*, 197(1):458–463, 2014. doi:10.1093/gji/ggt516.

Sallarès, V., Gailler, A., Gutscher, M.-A., Graindorge, D., and Bartolomé, R. e. a. Seismic evidence for the presence of Jurassic oceanic crust in the central Gulf of Cadiz (SW Iberian margin). *Earth and Planetary Science Letters*, 311:112–123, 2011. doi: 10.1016/j.epsl.2011.09.003.

Simões, J. Z., Afilhado, A., and Mendes Vitor, L. Assessing the tsunami risk instrumental and historical records. *Sci. TSUNAMI HAZARDS*, 10, 1992.

Stich, D., Mancilla, F. d. L., and Morales, J. Crust-mantle coupling in the gulf of cadiz (sw-iberia). *Geophysical Research Letters*, 32(13), 2005. doi: 10.1029/2005GL023098.

Terrinha, P., Matias, L., Vicente, J., Duarte, J., Luis, J., Pinheiro, L., Lourenco, N., Diez, S., Rosas, F., Magalhaes, V., Valadares, V., Zitellini, N., Roque, C., and Mendes Víctor, L. Morphotectonics and strain partitioning at the Iberia-Africa plate boundary from multibeam and seismic reflection data. *Marine Geology*, 267:156–174, 2009. doi:10.1016/j.margeo.2009.09.012.

Thiebot, E. and Gutscher, M.-A. The Gibraltar Arc seismogenic zone (part 1): Constraints on a shallow east dipping fault plane source for the 1755 Lisbon earthquake provided by seismic data, gravity and thermal modeling. *Tectonophysics*, 426:135–152, 2006. doi: 10.1016/j.tecto.2006.02.024.

Zitellini, N. and et al. The quest for the Africa–Eurasia plate boundary west of the Strait of Gibraltar. *Earth and Planetary Science Letters*, 208:13–50, 2009. doi:10.1016/j.epsl.2008.12.005.

A Stations metadata information

In this appendix we present the information about seismic stations.

In Table 1 on page 34 we have the information about OBS stations, and in Table 2 on page 35 we have the information about land stations.

Table 1: Information about OBS stations

Station name	Latitude (°)	Longitude (°)	Altitude (m)	Sampling interval (s)	Acquisition time (mm-dd hh:mm:ss.sss) Start time	End time	Data completeness of each component (%) Comp. 1	Comp. 2	Comp. 3	Comp. 4
31	35.7933	-7.1083	-1181	0.02	03-07 00:00:01.000	07-21 16:00:58.980	0.0	100.0	100.0	100.0
32	35.7167	-7.6083	-1455	0.01	01-21 23:59:59.000	07-21 17:59:58.990	100.0	100.0	100.0	100.0
33	35.8667	-7.9167	-1498	0.02	01-22 00:00:01.000	07-21 20:00:59.980	100.0	100.0	100.0	100.0
34	35.6467	-8.1733	-1840	0.01	01-22 00:00:00.000	07-21 17:59:59.990	97.3	97.3	97.3	97.3
35	35.7500	-8.5000	-2455	0.02	01-22 00:00:00.000	07-22 00:00:57.980	100.0	0.0	0.0	0.0
36	35.5500	-8.7167	-2839	0.01	01-22 00:00:00.000	07-22 00:59:59.990	100.0	100.0	100.0	100.0
37	35.5100	-9.1500	-3512	0.02	01-22 00:00:01.000	07-22 05:00:58.980	100.0	0.0	100.0	100.0
38	35.4200	-9.3667	-3544	0.02	02-27 00:00:01.000	07-22 00:00:58.980	100.0	100.0	100.0	100.0
39	35.5100	-9.5900	-4039	0.02	01-22 00:00:01.000	04-17 15:52:51.980	100.0	100.0	100.0	100.0
40	35.6000	-9.3700	-3786	0.02	01-22 00:00:00.000	07-22 10:00:57.980	100.0	100.0	0.0	100.0
41	35.6900	-9.5900	-4299	0.02	01-22 00:00:00.000	06-03 11:07:07.980	100.0	100.0	100.0	100.0
42	35.7800	-9.3700	-4081	0.02	01-22 00:00:00.000	07-22 14:00:56.980	100.0	100.0	100.0	100.0
43	35.6900	-9.1500	-3567	0.02	01-22 00:00:01.000	07-22 16:00:57.980	65.4	65.4	65.4	65.4
44	35.8000	-8.9333	-3381	0.02	01-22 00:00:01.000	07-22 17:00:58.980	100.0	100.0	0.0	100.0
45	36.0167	-8.7217	-3228	0.02	01-22 00:00:00.000	07-22 20:00:57.980	100.0	100.0	100.0	0.0
46	36.0167	-8.4417	-2477	0.02	01-22 00:00:01.000	07-22 22:00:58.980	100.0	0.0	0.0	100.0
47	36.0483	-8.1650	-1810	0.02	01-22 00:00:01.000	05-29 07:32:48.980	100.0	100.0	100.0	100.0
48	36.2500	-7.8833	-1080	0.02	01-22 00:00:00.000	07-21 23:53:47.980	100.0	100.0	100.0	100.0
49	36.2333	-8.1667	-1458	0.02	01-22 00:00:00.000	04-18 21:15:30.980	0.0	100.0	100.0	100.0
50	36.2733	-8.4417	-1752	0.01	01-22 00:00:00.000	07-23 05:30:36.990	100.0	100.0	100.0	100.0
51	36.2750	-8.7217	-2233	0.02	01-22 00:00:00.000	07-23 00:00:56.980	100.0	100.0	100.0	100.0
52	36.2333	-9.0000	-3034	0.01	01-21 23:59:59.000	07-23 07:59:58.990	100.0	100.0	100.0	100.0
53	36.5000	-8.7200	-1274	0.02	01-22 00:00:01.000	06-27 03:42:08.980	100.0	100.0	100.0	100.0
54	36.4317	-8.3400	-1161	0.02	01-22 08:09:46.000	04-11 01:00:00.980	100.0	100.0	100.0	100.0

Table 2: Information about land stations

Network	Station name	Longitude (°)	Latitude (°)	Sampling interval (s)
8A	PW20	-8.3563	38.5326	0.01
ES	EBAD	-7.0133	38.7556	0.01
ES	ECEU	-5.3768	35.8978	0.01
ES	EGRO	-7.4831	37.5342	0.01
ES	EMIN	-6.6724	37.7675	0.01
ES	ESPR	-5.8562	36.8686	0.01
IP	PACT	-8.83	38.77	0.01
IP	PMST	-9.18	38.74	0.01
LX	GGNV	-9.1492	38.7165	0.01
LX	MESJ	-8.21993	37.839752	0.01
LX	MORF	-8.6508	37.3063	0.01
PM	PBAR	-7.039	38.1745	0.01
PM	PBDV	-7.931167	37.243	0.01
PM	PCVE	-8.039	37.632833	0.01
PM	PESTR	-7.590167	38.867167	0.01
PM	PFVI	-8.826833	37.132833	0.01
PM	PMAFR	-9.282667	38.955333	0.01
PM	PMTG	-8.225333	39.069	0.01
PM	PNCL	-8.529	38.111833	0.01
PM	PVAQ	-7.717333	37.403667	0.01
WM	EVO	-8.013	38.532	0.01
WM	BARR	-7.3991	38.474	0.01
XB	PM01	-5.6543	35.7016	0.01
XB	PM03	-5.7713	35.5104	0.01
XB	PM04	-5.1525	35.4026	0.01
XB	PM05	-5.3368	35.2134	0.01
XB	PM06	-5.639	35.3086	0.01
XB	PM07	-4.9863	35.2275	0.01
XB	PM09	-5.1145	35.0273	0.01
XB	PM10	-5.1368	34.7379	0.01
XB	PM14	-5.1267	34.5522	0.01
XB	PM17	-5.2954	34.3914	0.01
XB	PS01	-5.6236	36.08	0.01
XB	PS02	-5.3708	36.2564	0.01
XB	PS03	-5.415	36.3932	0.01
XB	PS04	-5.3228	36.6051	0.01
XB	PS05	-5.0938	36.6457	0.01
XB	PS06	-5.5144	36.7314	0.01
XB	PS09	-5.2325	36.8235	0.01
XB	PS10	-4.9044	36.8025	0.01
XB	PS12	-5.1867	37.0506	0.01
XB	PS14	-5.5178	37.1475	0.01
XB	PS16	-5.0491	37.2131	0.01
XB	PS17	-5.3916	37.2934	0.01
XB	PS19	-4.9943	37.3716	0.01
XB	PS41	-5.9442	36.667	0.01
XB	PS42	-5.0434	36.5282	0.01
XB	PS44	-5.9889	36.3173	0.01
XB	PS51	-4.8873	36.973	0.01

B Networks of the seismic stations

In this appendix we present a brief description of the networks: the stations used from each, the operating time and institution behind them. Apart from the OBS network, all the information was obtained in the FDSN platform.

The temporary networks:

- **TM:** the network of OBS do not has an official name but in the this work it was called TM due its project (TOPO-MED). The OBSs were deployed in the offshore Cadiz Basin and were official operating between 22/01/2010 and 23/07/2010 – Grevemeyer (2011).
- **8A:** we used 1 of the 21 stations deployed in Portugal within the project West Iberia Lithosphere and Astenosphere Structure (WILAS). This network was operated by Instituto Dom Luiz, from 01/01/2010 to 31/12/2012.
- **XB:** we used 27 of the 93 stations deployed in Spain and Morocco, within the Program to Investigate Convective Alboran Sea System Overturn. This network was operated by University of Oregon, from 01/01/2009 to 31/12/2013.

The permanent networks:

- **ES**: we used 5 stations of the Spanish Digital Seismic Network, operated by Subdireccion General De Geodesia Y Geofisica in Spain, from 01/01/2000.
- **IP**: we used all the 2 stations of the Instituto Superior Tecnico Broadband Seismic Network, operated by this Institute in Portugal, from 01/01/2002.
- **LX**: we used all the 3 stations of the University of Lisbon Seismic Network, operated by this University in Portugal, from 01/01/1997.
- **PM**: we used 9 stations of the Portuguese National Seismic Network, operated by Instituto Português do Mar e da Atmosfera (IPMA) in Portugal, from 01/01/2006.
- **WM**: we used 2 of the 22 stations of the Western Mediterranean Seismic Network, operated by Real Instituto y Observatorio de la Armada, in Portugal, Spain and Morocco, from 01/01/2001.

C Velocity models

C.1 3D velocity model

We adapted the 3D velocity model from Arroucau and Custódio (2015) to created the 3D slowness grid used in LOKI and NonLinLoc. This velocity model, written in netCDF format, includes all the area presented in Figure C.1, and its nodes are arranged in approximately every 10 km in East-West and North-South directions, and 1 km in vertical direction.

As we wanted a resolution of 1 km in all directions, this grid was rearranged to serve that. In the end we got a 3D grid with 1 km space between nodes in all directions, with dimensions of $520 \times 370 \times 80$ km to be used in LOKI, and $580 \times 570 \times 80$ km to be used in NonLinLoc – Figure C.1

This information was written to a binary files, ready to be read by LOKI and NonLinLoc programs.

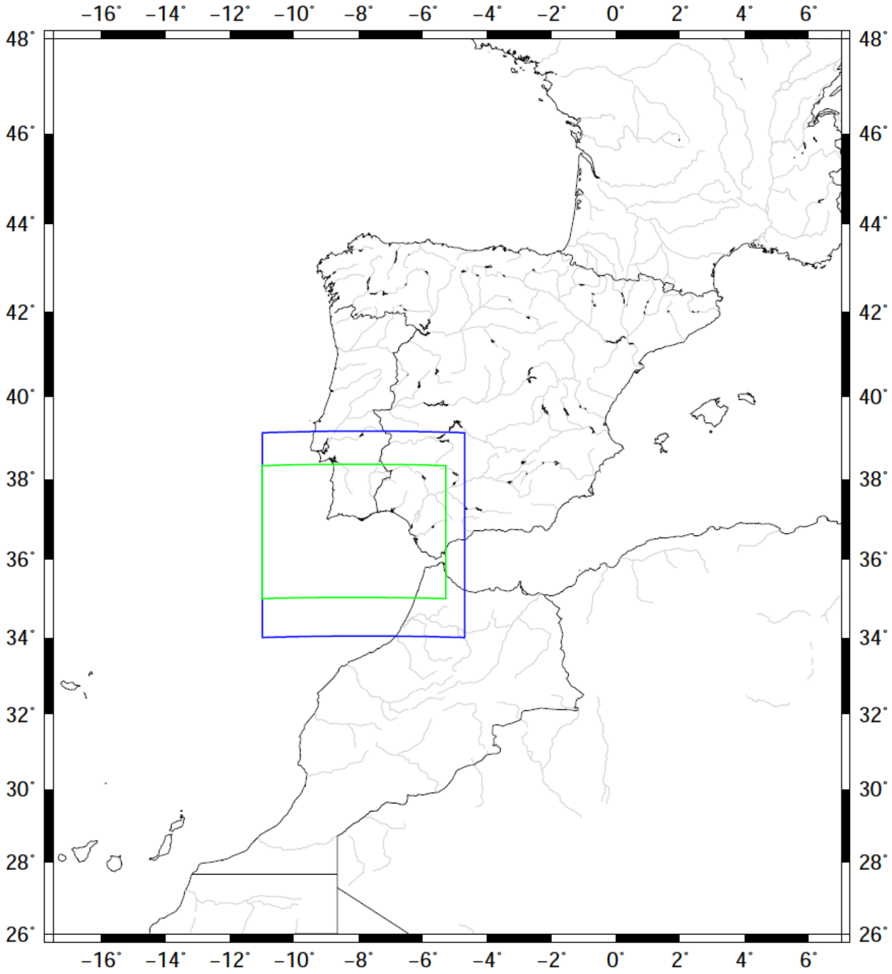

Figure C.1: Region included by the velocity model of Arroucau and Custódio (2015), and boundaries of the regions of interest used in LOKI (green rectangle) and NonLinLoc (blue rectangle).

C.2 1D velocity model

We used the velocity model from Geissler et al. (2010), presented below in Table 3, in the Vel2Grid program of NonLinLoc, to locate earthquakes.

Table 3: 1D velocity model from Geissler et al. (2010), with a Vp/Vs ratio of 1.77.

Depth below mean sea level (km)	Vp (km/s)	Vs (km/s)
0.0	2.200	1.243
6.5	3.800	2.147
10.0	5.800	3.277
13.0	6.500	3.672
16.0	7.900	4.463
20.0	8.100	4.576
27.5	8.150	4.605
35.0	8.200	4.633
42.5	8.250	4.661
50.0	8.300	4.689
60.0	8.350	4.718
70.0	8.400	4.746
75.0	8.450	4.774